Visualizing the interior architecture of focal adhesions with high-resolution traction maps

Masatoshi Morimatsu[a], Armen H. Mekhdjian[a]*, Alice C. Chang[a], Steven J. Tan[a], and Alexander R. Dunn[a, b]*

**These authors contributed equally*

Author Address

(a) Department of Chemical Engineering, Stanford University, Stanford, CA 94305.

(b) Stanford Cardiovascular Institute, Stanford University School of Medicine, Stanford, CA 94305.

Corresponding author

Alexander R. Dunn alex.dunn@stanford.edu Fax: (650)723-9780

Keywords

Mechanobiology, integrin, focal adhesion, molecular tension sensor, super-resolution, traction force microscopy

Supporting Information

Materials and Methods

Cell Culture

Human foreskin fibroblast (HFF) cells CCD-1070Sk (ATCC CRL-2091) were cultured in DMEM high glucose medium (Gibco, Cat #21063-029) in the absence of phenol red and supplemented with 10% fetal bovine serum (FBS, Axenia Biologix), sodium pyruvate (1 mM, Gibco), MEM non-essential amino acids (1x, Gibco), and penicillin/streptomycin (100 U/mL and 100 µg/mL, Gibco). The cells were incubated at 37 °C with 5% CO_2. On the day of the experiment, cells were washed with phosphate-buffered saline (PBS) (Gibco), trypsinized using 0.25% Trypsin-EDTA (Gibco), seeded on MTS-functionalized coverslips in a custom-made chamber, and allowed to adhere for ~60 minutes in DMEM high glucose media with 10% FBS. FRET measurements were made within 3 hours of plating the cells. Control measurements indicated that cells remained viable for at least 5 hours under experimental conditions, and that the MTSs did not detach from the coverslip surface in that time.

Fluorescent proteins and transfection

Stable cell lines: DNA constructs were transfected using Amaxa® Human Dermal Fibroblast Nucleofector® Kit (Lonza) using their optimized protocols. To achieve stable cell lines expressing paxillin (GFP at C-terminus) and myosin regulatory light chain (MRLC), we cloned these constructs into DNA 2.0's PiggyBac expression vectors. We changed the media to DMEM high glucose medium with no FBS and no antibiotics the night before transfection to increase transfection efficiency. One day after transfection, 1.0 µg/mL puromyocin was added to the media to select for stably transformed cells. Fresh media with drug was added after 2 days. The cells were then washed with PBS, and fresh media (with no drug) was added. Fluorescence images confirmed that ~75% of the resulting cells stably expressed the GFP-fusion proteins.

Transient expression: Cells were transfected using the Amaxa® Human Dermal Fibroblast Nucleofector® Kit, switching to DMEM high glucose medium with no FBS and no antibiotics the night before transfection. Cells were used 1-3 days post transfection. Actin-GFP was labeled using the appropriate CellLight® fluorescent protein construct (Life Technologies, Cat #C10582), with the manufacturer-specified protocol. GFP-tagged fusions of talin (GFP at N-terminus), vinculin (GFP at N-terminus), α-actinin (GFP at C-terminus), α_5 integrin (two versions; high and reduced expression, GFP at C-terminus) were obtained from Addgene (Plasmid #26724, 50513, 11908, 15238, 30450, respectively). mEmerald-tagged α_v integrin (mEmerald at C-terminus) was obtained from Addgene (Plasmid #53985). All of the GFP fusion proteins used in this work are either identical or functionally equivalent (i.e. GFP fusion in the same location) to constructs used in previous publications[1,2]. The α_5-GFP integrin construct we use has been used before[2-8]. The α_V-mEmerald construct is in the Addgene repository under Michael's Davidson's unpublished constructs, but similar constructs in which the fluorescent protein is attached at the C-terminus of α_V integrin have been used before[9-11]. We note that GFP-tagged integrins show similar localization patterns to those observed using immunocytochemistry to visualize the endogenous proteins in untransfected cells (Fig. 2; see also Ref. 12).

MTS Protein Expression and Purification

The DNA encoding the MTS was synthesized and cloned into the pJ414 bacterial expression vector (DNA 2.0). The MTS construct consists of a substrate binding site (a mutated Halo-Tag with two cysteines replaced with serines), an acceptor labeling site (TAG stop codon for incorporation of unnatural amino acid 4-Azido-L-phenylalanine), an elastic protein spring ($(GPGGA)_8$), a donor labeling site (Lys-Cys), and an integrin binding site (TVYAVTGRGDSPASSAA) (Figure 1). The amino acid sequence is

MGSEIGTGFPFDPHYVEVLGERMHYVDVGPRDGTPVLFLHGNPTSSYVWRNIIPHVAPTHRSIAPDLIG
MGKSDKPDLGYFFDDHVRFMDAFIEALGLEEVVLVIHDWGSALGFHWAKRNPERVKGIAFMEFIRPI
PTWDEWPEFARETFQAFRTTDVGRKLIIDQNVFIEGTLPMGVVRPLTEVEMDHYREPFLNPVDREPL
WRFPNELPIAGEPANIVALVEEYMDWLHQSPVPKLLFWGTPGVLIPPAEAARLAKSLPNAKAVDIGPG
LNLLQEDNPDLIGSEIARWLSTLEISGGAGEFGA(TAG)GPGGAGPGGAGPGGAGPGGAGPGGAGPGGAG
PGGAGPGGAKCAGSENLYFEQGTVYAVTGRGDSPASSAAHHHHHH

The pJ414-MTS and pEVOL-pAzF plasmids (Addgene Plasmid #31186)[13] were transformed into chemically competent BL21 DE3 *E. coli* cells. The cells were grown to an optical density (OD) of 0.8 at 37 °C in the presence of ampicillin, chloramphenicol, and 0.2% glucose. At an OD of 0.2, 1 mM 4-Azido-L-phenylalanine (Chem-Impex International, Inc.) was added. MTS protein expression was induced by adding L-arabinose to a final concentration of 0.02 % (w/v) at an OD of 0.4, and isopropyl β-D-1-thiogalactopyranoside (IPTG) to a final concentration of 1 mM at an OD of 0.8. Cells were then shaken at 220 rpm for 16 hours at 30 °C, and harvested by centrifuging at 6000xG at 4 °C for 30 minutes. The cell pellet was resuspended in lysis buffer (50 mM sodium phosphate, 300 mM NaCl, 10 mM imidazole, pH 8.0). 10 µM lysozyme, 2.0 U/ml DNAse I, 2 µM pepstatin, 5 µM leupeptin, and 100 µM phenylmethylsulfonyl fluoride were added to the suspension and gently mixed at 4 °C for 45 minutes. The mixture was sonicated on ice for 5 cycles for 60 seconds (pulsing at 1 second on/off intervals) and then centrifuged at 12000xG at 4°C for 30 minutes. HisPur Ni-NTA Resin (Thermo Scientific, Prod #88222) was added to the supernatant and gently mixed at 4°C for 2 hours. The protein was then purified using His-Tag affinity gravity flow chromatography. Briefly, settled resin was washed twice with 5 mL of wash buffer (50 mM sodium phosphate, 300 mM NaCl, 20 mM imidazole, pH 7.4), and then eluted with 4 mL of elution buffer (50 mM sodium phosphate, 300 mM sodium chloride, 250 mM imidazole, pH 8.0). Eluted protein was dialyzed overnight into 100 mM phosphate buffer (pH 7.0) using Dialysis Cassette Kit, MWCO 10K (Thermo Scientific). Samples were run on SDS-PAGE and analyzed by ESI-MS to verify full-length expression and purity (Figure S1). Protein concentration was determined using the Bradford assay and absorbance at 280 nm. The MTS protein was flash frozen and stored in aliquots at -80 °C.

Mass spectrometry

Unlabeled MTS (~50 µM) was diluted 1:10 with water containing 0.1% TFA and analyzed by ESI-MS (electrospray ionization mass spectrometry) with an Agilent 1260 HPLC and Bruker MicroTOF-Q II (Figure S1A). The gradient was 95% solvent A (0.1% TFA acid in water) held 2 minutes then ramped to 95% solvent B (0.1% TFA acid in acetonitrile) in 10 minutes. The column was a Zorbax 300SB-C8 2x100mm. The observed mass of the protein is 40,812 Da as shown in Figure S1 (expected molecular weight: 40,972 Da). The discrepancy may

be due to the removal of the N-terminal methionine (~130 Da) during expression, and a loss of N_2 (~28 Da) from the unnatural amino acid during the mass spectrometry measurement.

MTS labeling with fluorescent dyes

The dye labeling steps consisted of a click chemistry reaction for the acceptor dye and a thiol-maleimide reaction for the donor dye. First, 500 µl of unlabeled MTS (~50 µM) was mixed with ATTO 647N (ATTO TEC Gmbh)-alkyne at a molar ratio of 1:5 (protein:dye). Next, the sample was mixed with a premixed solution of 500 µM $CuSO_4$ (Sigma Aldrich) and 2.5 mM THPTA (3 [tris(3-hydroxypropyltriazolylmethyl)amine, Sigma Aldrich), 5 mM aminoguanidine (Sigma Aldrich), and 5 mM sodium ascorbate (Fluka), and incubated for 60 min at room temperature on a shaker. 5 mM EDTA (pH 8.0) and 1 mM TCEP were added to stop the click chemistry reaction and reduce any disulfide bonds that had formed. Next, the solution was exchanged into 100 mM phosphate buffer (pH 7.0) with a PD Mini Trap G-25 column (GE Healthcare Life Science). The sample (~20 µM) was mixed with Alexa 546 maleimide at a molar ratio of 1:3 (protein:dye) and incubated for 1 h at room temperature and overnight at 4°C. The solution was exchanged using a PD Mini Trap G-25 into Buffer A (20 mM Tris-HCl, 1 mM DTT, pH 8.0) in preparation for FPLC. The double-labeled sample was purified with ion-exchange chromatography on a MonoQ PC 1.6/5 column with an AKTA FPLC (GE Healthcare Life Science), using a 1.0 M NaCl linear gradient (10 mM/mL). The labeling efficiency of FPLC fractions containing both Alexa 546 and ATTO 647N was >95% (Alexa 546) and ~60% (ATTO 647N) as measured by UV-Vis absorption (Figure S1E). Counting molecules in the donor and acceptor channels to quantify the degree of colocalization shows that ~70% of MTSs have both dyes.

PEG-coated coverslip preparation

Coverslips (Fisher Brand, No. 1.0) were washed consecutively with 2-propanol, 5 M KOH, and methanol in a sonication bath for 20 minutes. Silanization of the glass was performed with 1% N-(2-aminoethyl)-3-aminopropyltrimethoxysilane (United Chemical Technologies) and 5% acetic acid in methanol for 30 min. Each coverslip was incubated with 8 mg maleimide-PEG-NHS (M.W. 5000, JenKem) in 50 µl 100 mM phosphate buffer (pH 7.0) for 1 h at room temperature. After washing with distilled water, coverslips were incubated with 3 mM Halo thiol ligand (Promega P6761) in 100 mM phosphate buffer (pH 7.0) overnight at room temperature. Finally, coverslips were washed with distilled water and stored at -20°C in a vacuum-sealed container.

Flow chamber assembly

Perfusion chambers (Grace Biolabs PC3L-1.0, Product #622103) were attached to PEGylated coverslips. 1 mM L-cysteine hydrochloride (Sigma Aldrich) was added for 10 minutes to quench un-reacted maleimide on the glass. Labeled MTS (~5 nM) was then added to the flow cell and incubated for 30 min, followed by Pluronic F-127 (0.2% w/v) for 5 minutes to prevent non-specific cell attachment. All above steps were preceded with a PBS wash to remove excess reagent from the prior step. HFFs were then added and incubated for 30-60 minutes at 37 °C in DMEM high glucose medium (see cell culture methods). Finally, the chamber was washed with DMEM high glucose media with 10% FBS and 2 mM Trolox (Sigma) before imaging.

Ensemble TIRF imaging

Ensemble fluorescence measurements were performed with objective-type total internal reflection fluorescence (TIRF) microscopy on an inverted microscope (Nikon TiE) with an Apo TIRF 100x oil objective lens,

NA 1.49 (Nikon). Fluorescent dyes were excited with 532 nm (Crystalaser) and 635 nm (Blue Sky Research) lasers. Emission from Alexa 546 and ATTO 647N was separated using custom-built optics. Key elements are a quad-edge laser-flat dichroic with center/bandwidths of 405 nm/60 nm, 488 nm/100 nm, 532 nm/100 nm, and 635 nm/100 nm from Semrock (Di01-R405/488/532/635-25x36) and corresponding quad-pass filter with center/bandwidths of 446 nm/30 nm, 510 nm/30 nm, 581 nm/30 nm, 703 nm/30 nm band-pass filter (FF01-446/510/581/703-25). The channels were split by a dichroic beam splitter (635 nm), and then passed through band-pass filters in both the donor channel (593 nm/40 nm) and in the acceptor channel (645 nm/30 nm). Donor and acceptor images were focused on the same camera chip. Data were acquired at 4 frames per second with an EMCCD camera (Andor iXon). GFP-fusion proteins were excited using a 473 nm (Coherent Obis) laser. In addition to passing through the quad-edge laser-flat dichroic/filter, we added an additional band-pass emission filter (593 nm/40 nm) in the donor emission path to cut out bleed-through of the GFP signal in the FRET channel. A motorized filter flip mount (Thor Labs) was used to switch in/out the second emission filter when imaging FRET and GFP (in/out respectively).

Antibodies

Mouse anti-integrin $\alpha_v\beta_3$ (Cat #MAB1976), mouse anti-integrin $\alpha_5\beta_1$ (Cat #MAB1999), and mouse anti-paxillin (Cat #05-417) were purchased from Millipore. Mouse anti-vinculin (Cat #V9264) and mouse anti-talin (Cat #T3287) antibodies were purchased from Sigma-Aldrich. Secondary anti-mouse and anti-rabbit IgG conjugated to Alexa 488 were purchased from Cell Signaling Technology (Product #4408S and #4412S, respectively). Rabbit anti-paxillin pY31 and pY118 were purchased from Life Technologies (Product #44-720G and #44-722G, respectively). Blocking antibodies P5D2 and L230 were generous gifts from Mallar Bhattacharya and Dean Sheppard (UCSF). Additional antibodies used were specific to α_5 integrin (Abcam, clone EPR7854, catalog #: ab150361) and α_v integrin (clone L230, gift from Mallar Battacharya).

Immunofluorescence Microscopy

Cells were fixed with a solution of 4% paraformaldehyde (Polysciences, Inc.) in PBS, permeabilized with a solution of 0.25% Triton X-100 in PBS and blocked with a solution of 1% BSA in PBS. Samples were then incubated with 1 µg/mL primary antibodies (diluted in 1% BSA) for 1-2 hours and then 1 µg/mL secondary antibodies (also diluted in 1% BSA) for 30-60 minutes. The samples were imaged using an inverted Ti-Eclipse TIRF microscope (see TIRF imaging, above). Image analysis was performed with ImageJ and MATLAB software.

Ensemble FRET calculations (FRET Index)

Ensemble FRET is reported as a FRET index as opposed to an absolute FRET efficiency since it is straightforwardly derived from the experimental data, and because relative, as opposed to absolute, FRET values are the experimentally meaningful quantities in this study. To calculate FRET index, we divide the acceptor intensity *A* (background subtracted) by the sum of the acceptor and donor (*D*) intensities (also background subtracted): $FRET = A/(A + D)$. Note that this index does not account for donor and acceptor fluorescence quantum yields or photon detection efficiencies[14]. Inverted FRET maps are calculated as:

$$\text{Inverted FRET} = \frac{F_b - FRET}{\max\,(F_b - FRET)}$$

where F_b is a background FRET index measured in regions without observable cell-generated tension. This is

done to make low FRET values (corresponding to high tension) appear as bright regions, allowing the reader to straightforwardly visualize cell-generated forces.

Correlation analysis between inverted FRET and GFP intensity

We calculated the spatial correlation and center-of-mass offsets for GFP-tagged FA proteins and FRET[15] using a custom MATLAB script. Our code first reads the GFP and FRET images (see Ensemble FRET calculations, above). Each image is background subtracted, averaged over 10 frames (2.5 seconds), and normalized by the maximum intensity in the resulting, averaged image. For the FRET image, the image is subtracted from the background FRET value (this is done because the background FRET is higher than the FRET in the regions that are under tension).

We next segmented the images to determine the locations of FAs suitable for analysis. Both images were first filtered using boxcar averaging ("moving_average v3.1" from MATLAB Central File Exchange). The resulting images have the same dimensions as the original images. To compensate for intensity differences in each cell due to variable GFP expression, an automatic program was written to loop through threshold values used to convert the boxcar-averaged images to binary images for both the GFP channel and FRET channel. The user defines the most appropriate threshold value after observing the results of segmentation analysis at each threshold value. The images are then segmented using a watershed algorithm (MATLAB function: *watershed*); additional scripts clean the segmentation analysis by combining adjacent islands and setting a lower limit on the size of an island (in our case this was 25 pixels total, or a 500x500 nm^2).

The resulting segmented FRET and GFP emission regions were hand-curated to exclude instances where the automated routine misidentified or misannotated FAs: examples include inappropriately merging adjacent FAs or missing either the FRET or GFP signal for a given FA. The spatial extent of an individual FA is defined as the union of the pixels from the segmented GFP and FRET index regions. The Pearson's correlation coefficient between FRET and the GFP intensity is calculated over this region. The edge and center of the cell was manually identified for each cell, allowing us to calculate the offset between the FRET and GFP centers of mass. Specifically, this offset is defined as the difference in vectors extending from the cell center to the FRET and GFP centers of mass. Please see Figure S17 for a detailed schematic of the analysis routine.

FRET index to FRET efficiency conversion

Converting from FRET index to FRET efficiency is necessary to extract quantitative values for force from the FRET efficiency to force calibration curve. However, the conversion from FRET index to FRET efficiency requires a number of assumptions, such as accurate measurement of labeling efficiency, bleed-through, and fluorescence background[16,17]. We calculated absolute FRET efficiencies using the following approach:

The FRET efficiency at the single-molecule level is given by the equation

$$E = \frac{(I_a)}{(I_a) + \gamma(I_d)} \qquad (1)$$

Where:

$I_a = acceptor\ intensity\ during\ FRET\ (background\ subtracted)$
$I_d = donor\ intensity\ during\ FRET\ (background\ subtracted)$

$I_{d0} = donor\ intensity\ after\ acceptor\ photobleaching\ (background\ subtracted)$

$$(2) \qquad \gamma = \frac{(I_a)}{(I_{d0} - I_d)}$$

Replacing the expression for γ (2) into (1) yields a donor-only equation for FRET efficiency:

$$(3) \qquad E = \frac{I_{d0} - I_d}{I_{d0}} = 1 - \frac{I_d}{I_{d0}}$$

$$(4) \qquad I_d = I_{d0}(1 - E)$$

Solving equation (1) for I_a in terms of I_d and E

$$(5) \qquad I_a = \frac{\gamma I_d E}{1 - E}$$

Substituting I_d from (4) into (5) yields

$$(6) \qquad I_a = \gamma I_{d0} E$$

At the ensemble level, the total intensity for donor and acceptor channels can be related to single-molecule parameters by:

$$(7) \qquad A_i - A_b = n\alpha I_a$$

$$(8) \qquad D_i - D_b = n\alpha I_d + n(1 - \alpha) I_{d0}$$

Where:

$A_i = ensemble\ acceptor\ intensity$
$D_i = ensemble\ donor\ intensity$
$A_b = ensemble\ acceptor\ background$
$D_b = ensemble\ donor\ background$
$\alpha = fraction\ of\ donor - labeled\ sensors\ that\ have\ an\ acceptor$
$n = number\ of\ fluorescing\ sensors$

Use of equations (4) and (6) yields:

$$(9) \qquad A_i - A_b = n\alpha I_a = n\alpha\gamma I_{d0} E$$

$$(10) \qquad D_i - D_b = n\alpha I_{d0}(1 - E) + n(1 - \alpha) I_{d0}$$

Solving for $FRET_i$ (ensemble FRET index), we get

$$FRET_i = \frac{A_i - A_b}{(A_i - A_b) + (D_i - D_b)} = \frac{n\alpha\gamma I_{d0} E}{n\alpha\gamma I_{d0} E + \gamma(n\alpha I_{d0}(1 - E) + n(1 - \alpha) I_{d0})}$$

$$(11) \qquad FRET_i = \frac{\gamma E}{\gamma E + \gamma\left((1 - E) + \frac{(1 - \alpha)}{\alpha}\right)}$$

Rearranging to get *E* (FRET efficiency) in terms of $FRET_i$ (FRET index)

$$E = \frac{FRET_i}{\alpha\,(\gamma - FRET_i\gamma + FRET_i)} \tag{12}$$

Thus, to convert to FRET efficiencies from FRET index values, we use this relationship and the experimentally determined value for γ (0.75). We also use the background FRET index values (where there is no cell) and the known no-load FRET efficiency (71%) to determine the best-fit value of α, which we find to be 80%, close to the value of 70% derived from single molecule counting.

Introduction to 3B Analysis

The 3B algorithm determines the positions of fluorophores based on patterns of blinking and bleaching events recorded in ~200-300 frame movies collected at 20 Hz[18]. We ran the 3B algorithm on virtual machines implemented on Amazon's EC2 cloud computing service[19]. Each calculation ran on the compute-optimized c1.large servers for approximately 10 hours. We found this to be quicker and cheaper as compared to Amazon's c1.medium servers, which run for at least 20 hours to complete an analogous analysis. We ran the 3B analysis on actin filaments attached to glass coverslips and find that the FWHM is 39.5 ± 3.1 nm (SEM) (Figure S23).

3B Analysis for FRET images

To our knowledge Bayesian localization microscopy has not been used in tandem with FRET measurements. 3B relies on the probabilistic analysis of the blinking and bleaching of fluorophores. The model utilized by 3B assumes only 3 states for a given fluorescent molecule, ON, Blinking, and OFF. Therefore, a number of conditions are necessary to make 3B suitable for localizing high force regions under our experimental conditions.

First, the acceptor dye attached to our sensor, Atto 647N, is extremely photostable[20]. After continuous illumination by the 532 nm laser for 96 seconds (480 frames at a 0.2 second exposure), we did not observe noticeable photobleaching of the acceptor along with a corresponding photorecovery of the donor. Instead, we saw that the signal in both channels decreased at the same rate, indicative of donor photobleaching. This is ideal for 3B, since the algorithm derives some of its information from bleaching events.

This observation led us to simplify the problem of applying 3B in the context of FRET. For a molecule containing a FRET pair, the donor dye has 4 possible states (FRETing, ON, Blinking, OFF). Herein FRET = functional donor and acceptor, ON = high intensity due to acceptor photobleaching, Blinking = donor temporarily switching to background intensity, OFF = donor permanently at background intensity. After confirming that the acceptor dye was stable during illumination with the 532 nm laser, we were able to simplify the problem to 3 possible donor states (FRETing, Blinking, OFF), matching the states used by the 3B analysis. Further, MTS molecules under no tension exhibit low levels of donor emission due to efficient FRET. Because of this, the 3B algorithm selectively identifies MTS molecules under tension.

Hence, the donor signal provides information about the force just as a single fluorophore would, provided the signal is sufficiently distinguishable from the background (see Quantification of 3B Analysis). With the donor signal, we can create super-resolved force maps showing regions of high load as detected by our MTSs.

The assumptions necessary for this analysis to be appropriate are the following:

1) Uniform distribution of MTS molecules on the surface.
2) Acceptor does not photobleach or change intensity over the course of the experiment.
3) FRETing molecules do not move.

Quantification of 3B Analysis

To measure the performance of the 3B algorithm in our experiment we examined the relationship between the signal-to-noise ratio of the original image and the output of the 3B analysis. To determine the signal-to-noise ratio for each image input to 3B, we created histograms for the intensity values from the images generated by summing over all the frames in the 3B movie. The histograms were then fit to 2 Gaussians for the FRET donor image. The two peaks correspond to pixels with fluctuations around the background, and pixels that show higher emission intensity due to FRET-dequenching that reflects local tension. The histogrammed GFP intensity distribution was fit to 3 Gaussians, reflecting background, FA-localized proteins, and the cytosolic GFP-tagged protein and/or cellular autofluorescence. The signal-to-noise ratio (SNR) for the FRET donor and GFP images was defined as:

$$Signal\text{-}to\text{-}Noise\ Ratio = \frac{Mean\ of\ Signal\ Peak - Mean\ of\ Background\ Peak}{Standard\ Deviation\ of\ Background}$$

This definition is useful because it incorporates both the absolute difference in the signal vs. background and the random fluctuations within the background signal. FRET donor SNR calculated in this way ranged between 1.9 to 4, while the GFP SNR ranged between 8 for vinculin to 20 for paxillin (Figure S24).

To calculate the sum-squared error (SSE), we first generated normalized FRET donor and GFP images. To do so, we: *i)* summed the frames from the 3B movie, *ii)* normalized the summed image by the number of frames, *iii)* subtracted the mean of the background peak as determined from the Gaussian fits above, and *iv)* normalized the resulting image by dividing by the maximum pixel intensity. For the 3B output, we likewise normalized by the maximum pixel intensity to create a meaningful comparison between the two images. We also binned the 3B output using the average intensity bin method (Fiji) to match the pixel size of the raw data. We then took the difference between the corresponding pixels in each image and calculated the summed-square difference for the normalized data and 3B images:

$$SSE = \frac{\sum_{i=1}^{x}\sum_{j=1}^{y}[m(i,j) - n(i,j)]^2}{\sum_{i=1}^{x}\sum_{j=1}^{y} m(i,j)}$$

where $m(i,j)$ is the normalized intensity for pixel (i,j) in the original image, $n(i,j)$ is the corresponding intensity in the 3B image, and x and y indicate the size of the image in pixels. To ensure a standardized metric, we normalized by the total intensity of the original image.

In an alternate approach, we convolved the 3B output with a 2D Gaussian representing the point spread function of our microscope before calculating the SSE, as above (Figure S24). For both the non-convolved and convolved 3B data, we see no statistical difference between the SSE's for images with a high vs. low SNRs, suggesting that the 3B algorithm localizes molecules in regions with high intensity with equal success with higher or lower signal/noise images (Figure S25).

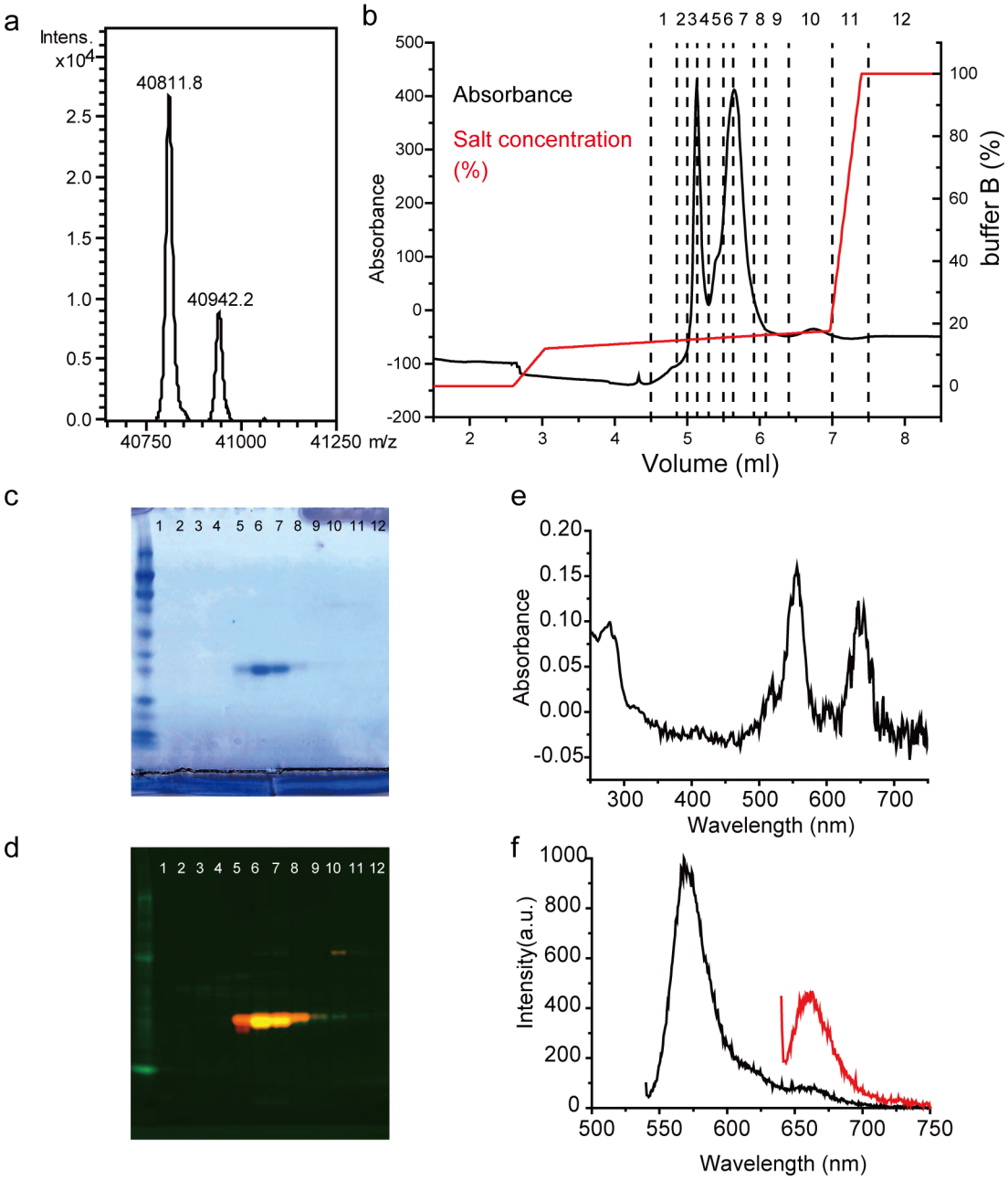

Figure S1. Biochemical characterization of MTSs. **a)** Deconvolved mass-spectrometry scan for unlabeled MTS. **b)** FPLC trace of dye-labeled MTSs. **c, d)** SDS-PAGE of FPLC fractions stained with Coomassie Blue (c) and imaged with a Typhoon 9410 fluorescence scanner (d) indicate that fractions 6 and 7 contain full-length MTSs labeled with both donor (green) and acceptor (red) dyes. **e)** UV-Vis absorption spectrum of double-labeled fractions. **f)** Emission spectrum of dye-labeled MTSs excited by 532 nm laser (black) and 635 nm laser (red) using a LS55 fluorimeter (PerkinElmer).

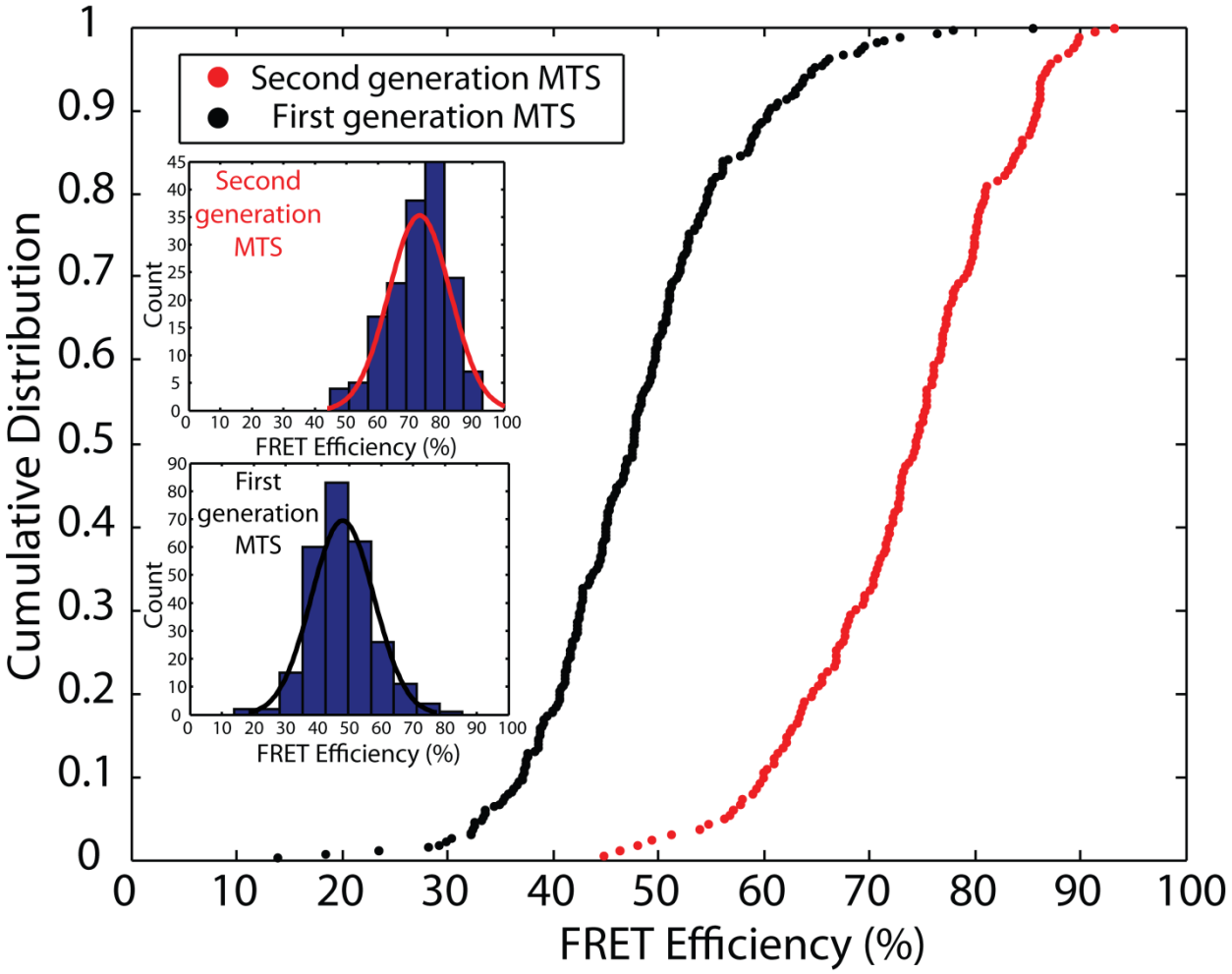

Figure S2. Single molecule FRET distribution at no load for current ("second-generation") and previously published MTS[21]. The average value for the single molecule FRET efficiency for the current sensor is ~71% vs. ~50% in the earlier design.

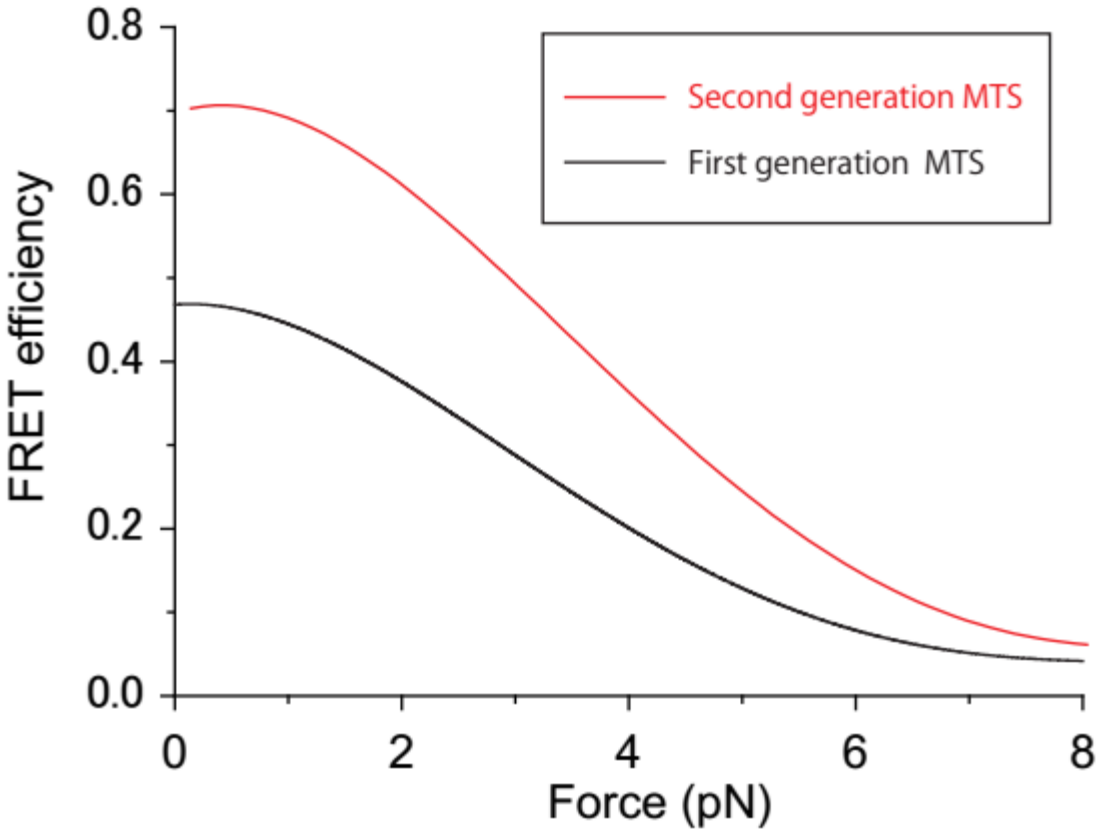

Figure S3. Theoretical calibration curves for previously published and current MTSs. These curves are based on the calibration obtained by Grashoff et al. (Nature 2010), corrected for the R_0 of the FRET pair used here and the experimentally determined resting FRET efficiency (Figure S1). The higher resting efficiency of the second generation MTS increases the dynamic range, allowing more accurate FRET measurements and an expanded force-sensitive range.

a

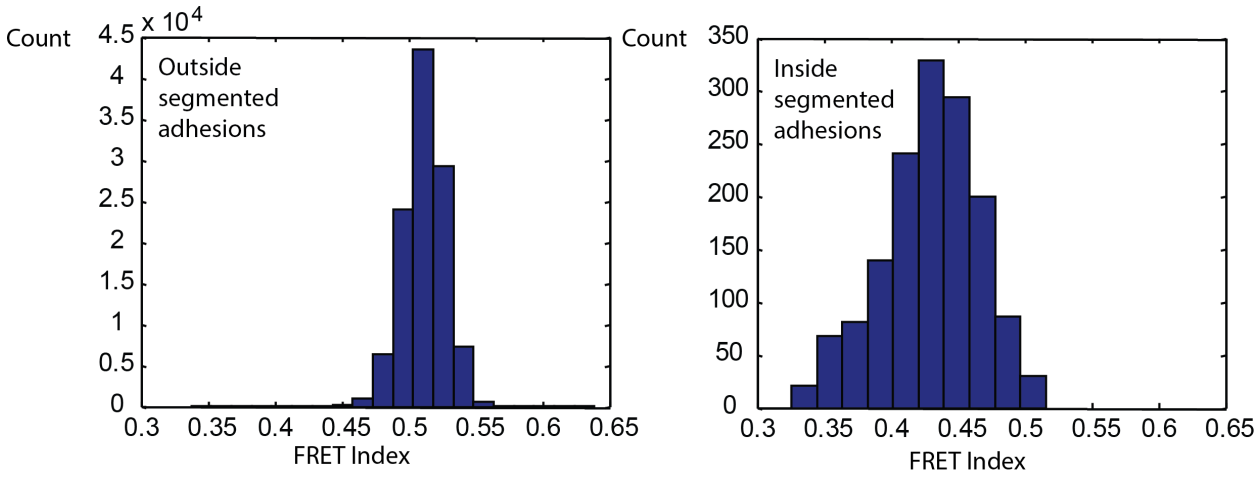

b

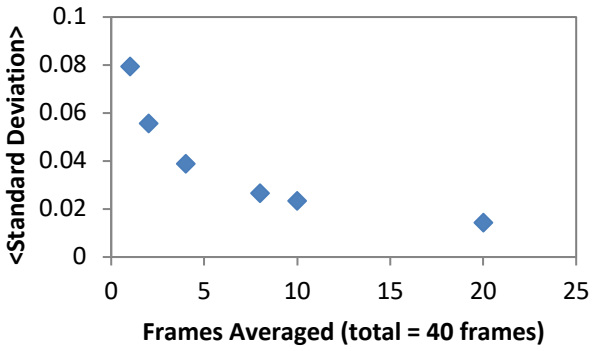

Figure S4. FRET index single-to-noise. **a)** An example dataset showing histograms of the FRET index (not efficiency) pixel values outside segmented adhesions compared with those inside segmented adhesions. These histograms illustrate the spread in FRET index values we obtain for "background" (FRET outside adhesions) and "signal" (FRET inside adhesions). The variability within adhesions is indicative of different local force levels. **b)** For a different dataset, we calculated the average donor and acceptor intensities in a field of view (donor: 2042.9 +/- 446.5 a. u., acceptor: 1971.6 +/- 441.6 a.u., the corresponding FRET index values (0.498 +/- 0.079), where the errors are the standard deviations. The total number of pixels analyzed here is 48,418. We then calculate how the average standard deviation of FRET index changes with averaging over a specific number of frames. The uncertainty in the FRET index for a given pixel asymptotes to ~0.02 for time-averaging over 4 or more seconds (10 frames).

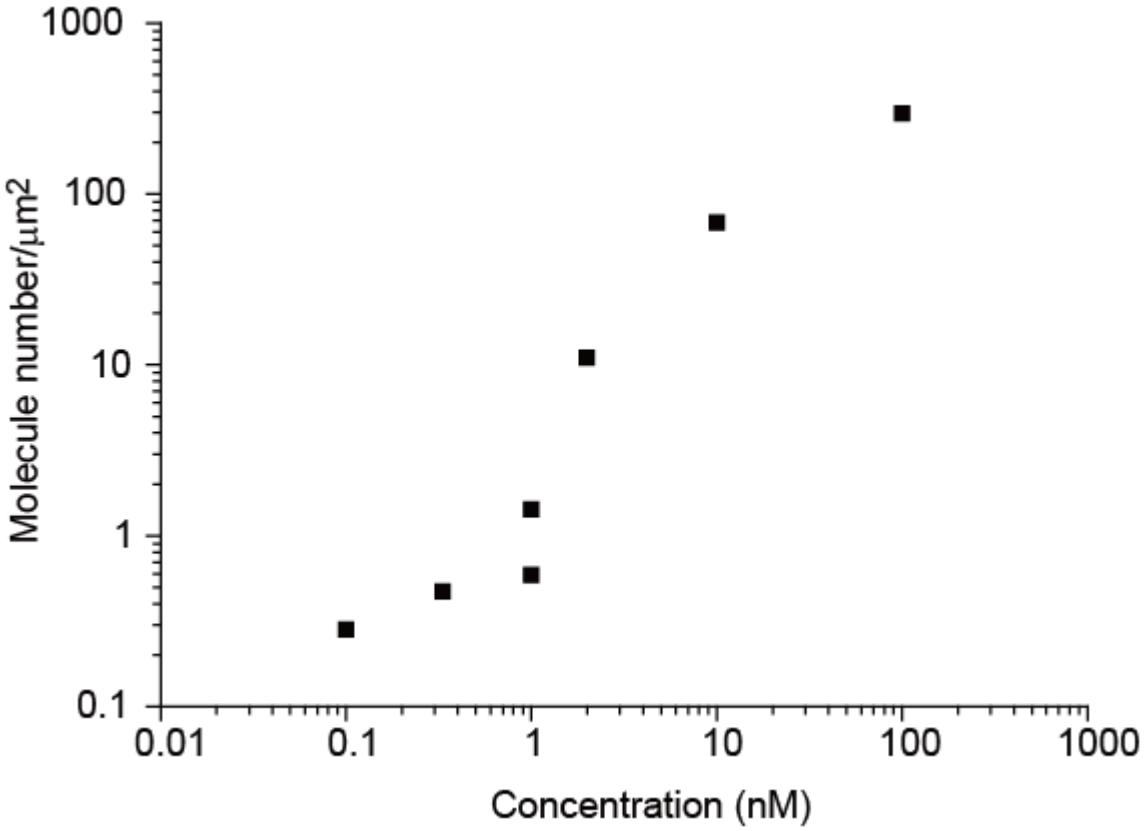

Figure S5. Determination of MTS surface density. Individual MTS molecules were directly observed at low added MTS concentrations (180 and 300 molecules were counted per 637 μm^2 field of view for the 0.1 and 0.3 nM concentrations, respectively). At 1 nM added MTS, single fluorophores were not initially resolved, but photobleaching resulted in a field of view where individual MTS molecules could be counted over time. Using this information, we calculated an effective intensity per molecule and extrapolated the surface MTS density by fitting the decay kinetics of the integrated fluorescence for the field of view to a single exponential decay plus a constant term, which reflected the background signal. For 2, 10, and 100 nM added MTS, we first recorded the background-subtracted integrated fluorescence intensity at multiple camera gain levels. We then compared these values to the integrated fluorescence intensity measured for 1 nM added MTS prior to photobleaching. Linking the single molecule and ensemble fluorescence data results in a linear relationship between the concentration of added MTS and the observed fluorescence signal. We used this fit to extrapolate the surface density of sensors at our working concentration of 50 nM.

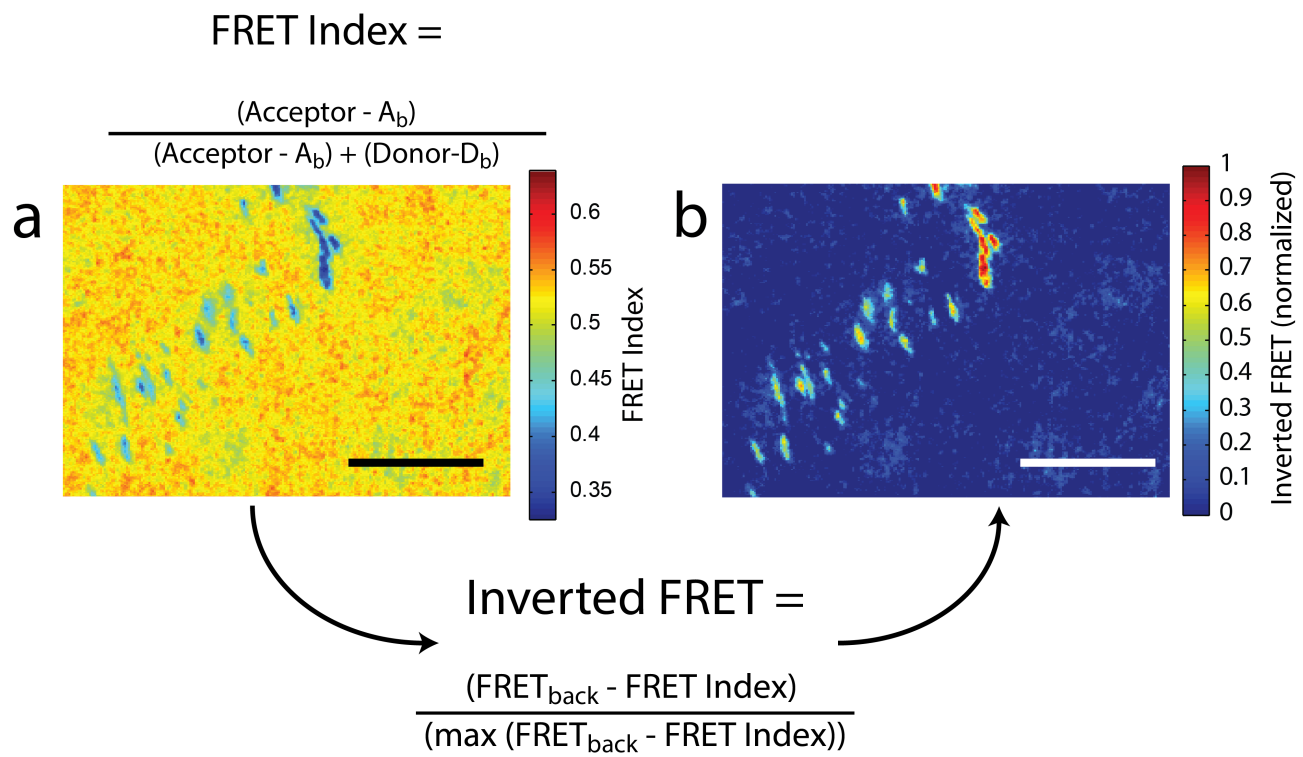

Figure S6. Calculating FRET index and the normalized, inverted FRET index. **a)** FRET Index map. **b)** Normalized, inverted FRET maps calculated from the FRET Index maps using the equation shown below. Scale bar in both images is 10 µm.

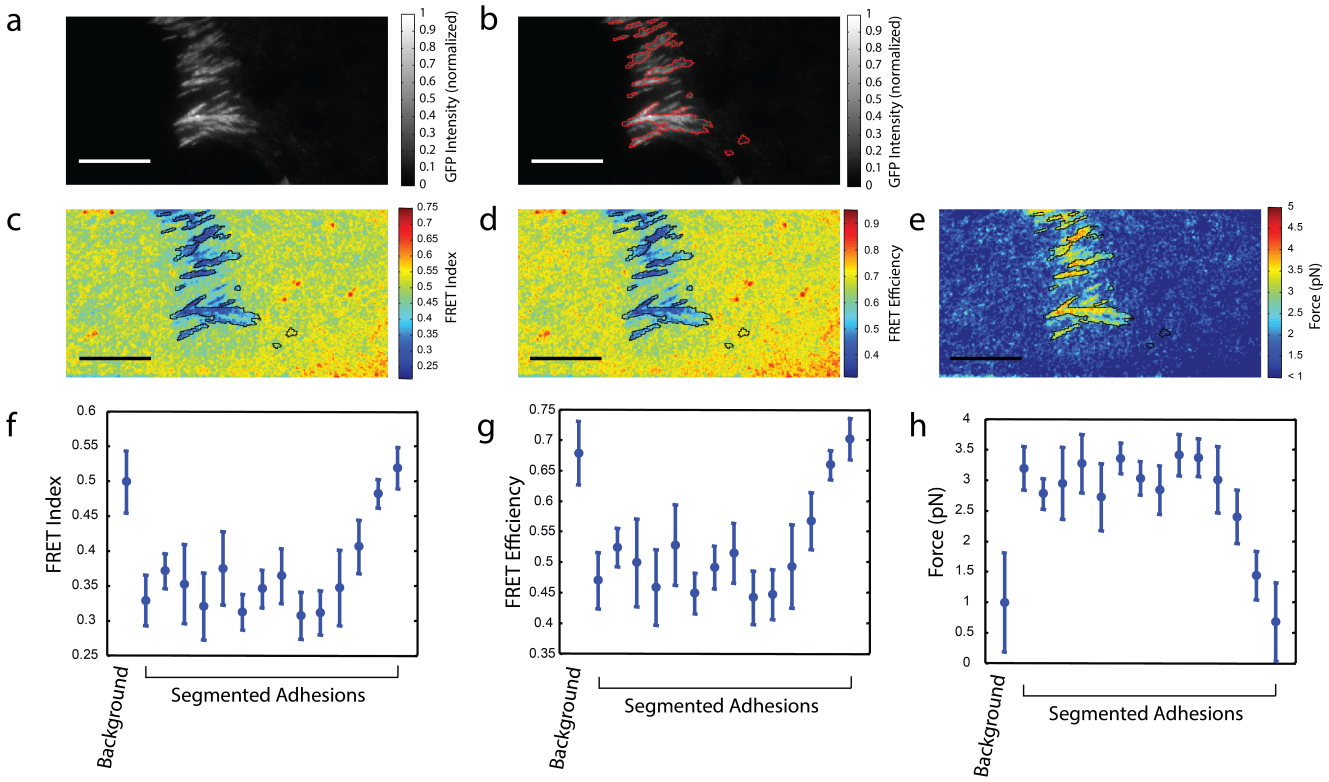

Figure S7. a) HFFs stably expressing GFP-paxillin visualized in TIRF with **b)** adhesions outlined in red. Adhesions are found using a watershed algorithm with manual determination of the threshold. **c)** FRET Index map for the corresponding cell. **d)** Using the calculations explained in *FRET index to FRET efficiency conversion*, we convert the FRET index map to a FRET efficiency map. **e)** We calculate the corresponding force map from the FRET efficiency map using the FRET vs. force calibration curve from Figure S2. **f)** Plot of the FRET Index values averaged for all pixels not within the adhesions in red (i.e. background FRET Index), and FRET Index values for the pixels within each of the adhesions outlined by red (from left to right). The error bars represent the standard deviation of FRET index values for the pixels. **g, h)** Corresponding FRET efficiency values (g) and force values (h) within the segmented adhesions. All scale bars are 10 µm.

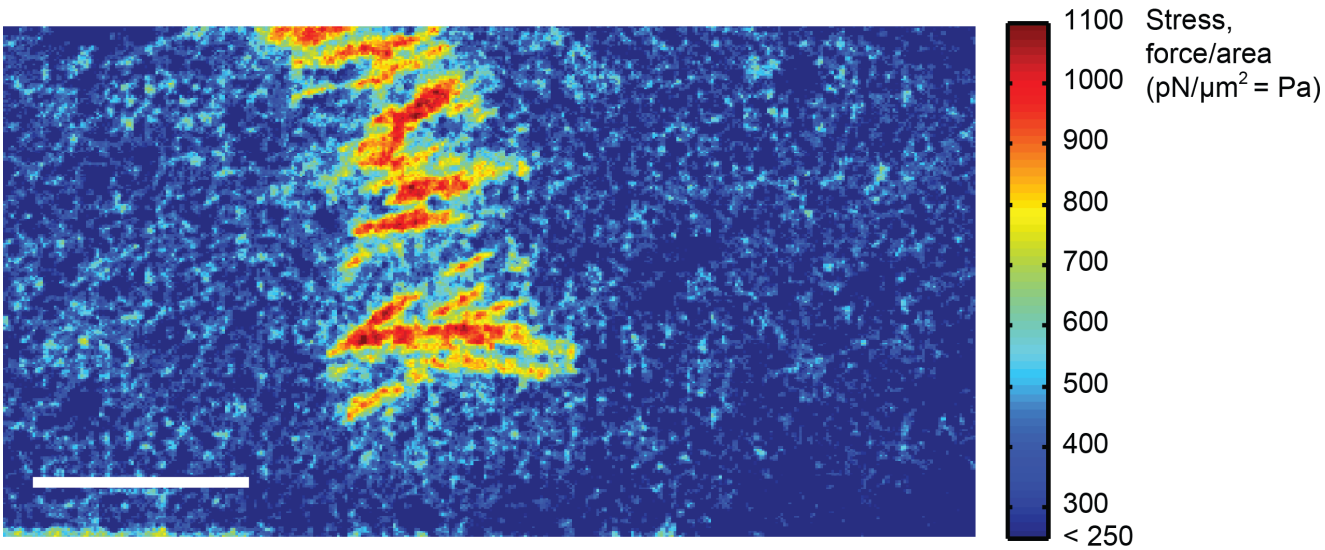

Figure S8. Calculated stress map. From our density calculations, we estimate that the number of molecules per pixel is ~2.5 (~150,000 molecules/637.5 μm^2, 0.01 μm^2/pixel). We can thus multiply each pixel force value by 2.5 to obtain a total force per pixel. We then divide by the pixel area (100 nm x 100 nm = 0.01 μm^2) to obtain the stress field, shown in units of Pa. Scale bar is 10 μm.

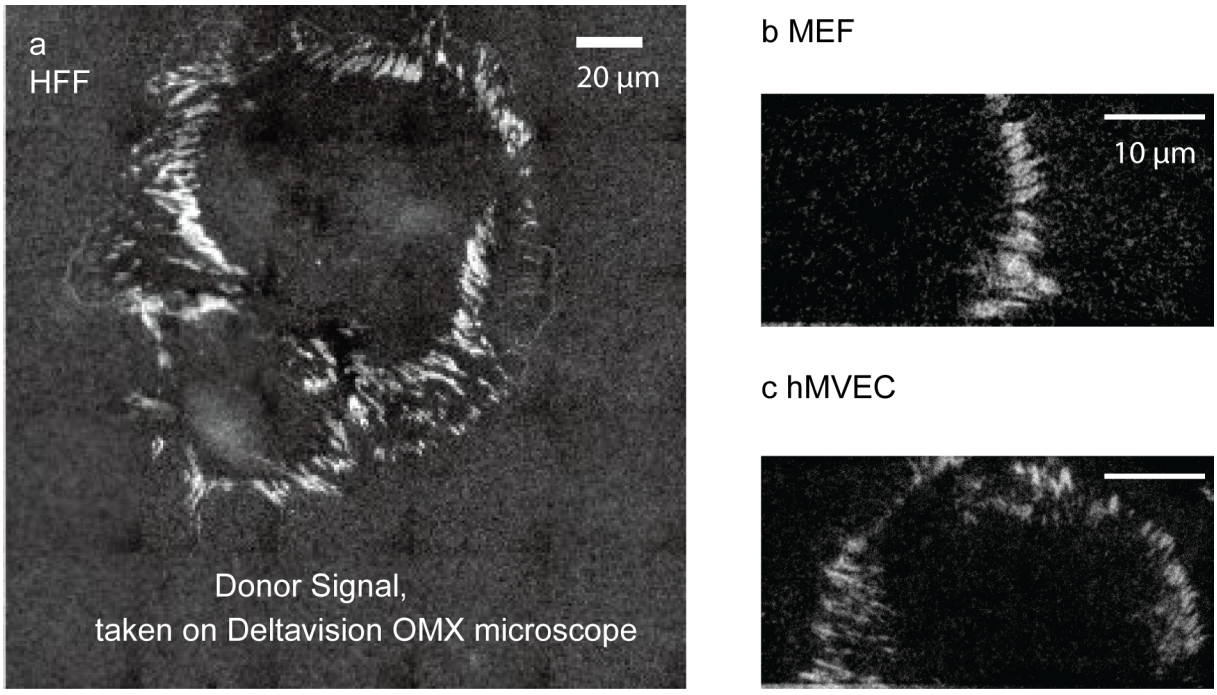

Figure S9. FRET maps for an entire HFF cell and for different cell types. **a)** Donor signal map taken on a Deltavision OMX microscope in mosaic mode. **b, c)** Inverted FRET maps for a mouse embryonic fibroblast (b) and human microvascular endothelial cell (c).

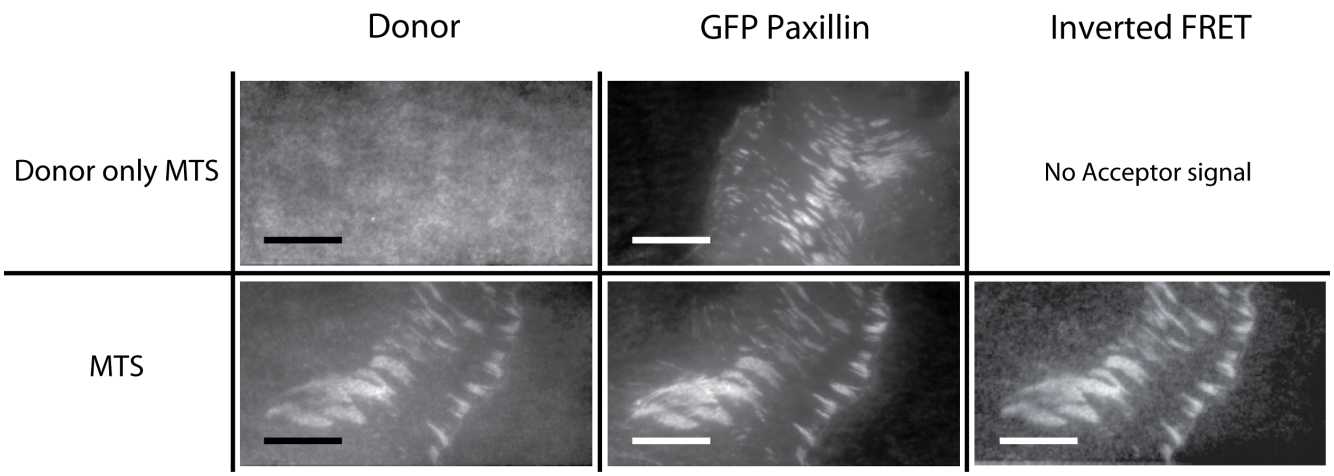

Figure S10. Control measurement with donor-only MTSs. Top row: sensors that only have the donor dye show no fluorescence intensity changes when a cell is present. Note also that the GFP signal does not bleed into the donor channel. Variations in donor signal intensity reflect local surface functionalization efficiencies and spatial variations in the illumination intensity. Bottom row: the donor channel for MTS sensors with both FRET donor and acceptor present shows clear increases in FRET at focal adhesions, as defined by GFP-paxillin recruitment. The inverted FRET signal (which is not defined in the absence of an acceptor signal), shows high intensity in locations in which paxillin is recruited (see *Ensemble FRET calculations*). All images were recorded using TIRF. Scale bar in all images is 10 μm.

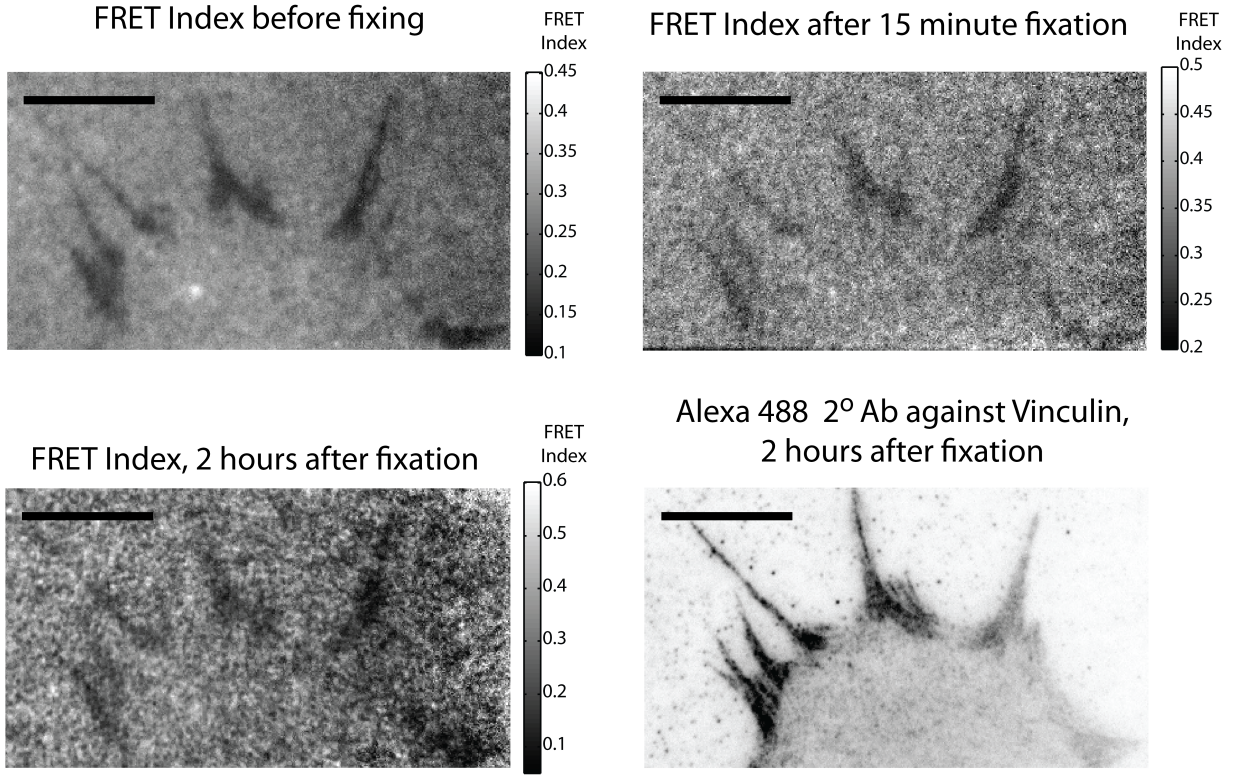

Figure S11. *In situ* fixing and staining of HFFs seeded on doubly-labeled MTSs. Chambers were prepared normally and the FRET signal was recorded using TIRF. Immediately afterwards, the flow cell was taped to the microscope stage and the cells were fixed with 4% paraformaldehyde. The staining process was carried out as described (see *Immunofluorescence Microscopy*), except that all incubation times were decreased by half. The FRET signal was checked after each subsequent solution addition to verify that the stage had not moved. Scale bar in all images is 10 µm.

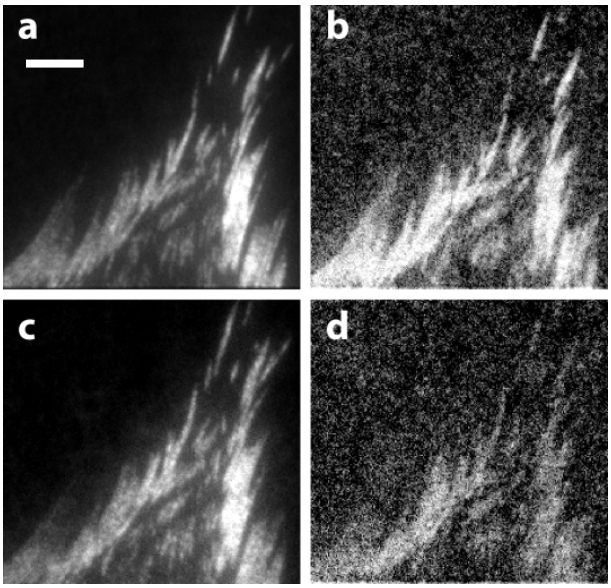

Figure S12. Testing for fixation artifacts on GFP and tension localization. HFF transfected with GFP-paxillin plated on MTS. **a)** GFP-paxillin before fixation. **b)** MTS inverted FRET before fixation. Bright white equals low FRET and high force. **c)** GFP-paxillin after fixation. **d)** MTS inverted FRET after fixation. Low FRET tracks paxillin both before and after fixation, and cell movement during fixation is minimal. Decrease in the FRET signal-to-noise ratio reflects photobleaching due in part to repeated exposures during this control experiment. Scale bar is 2 μm.

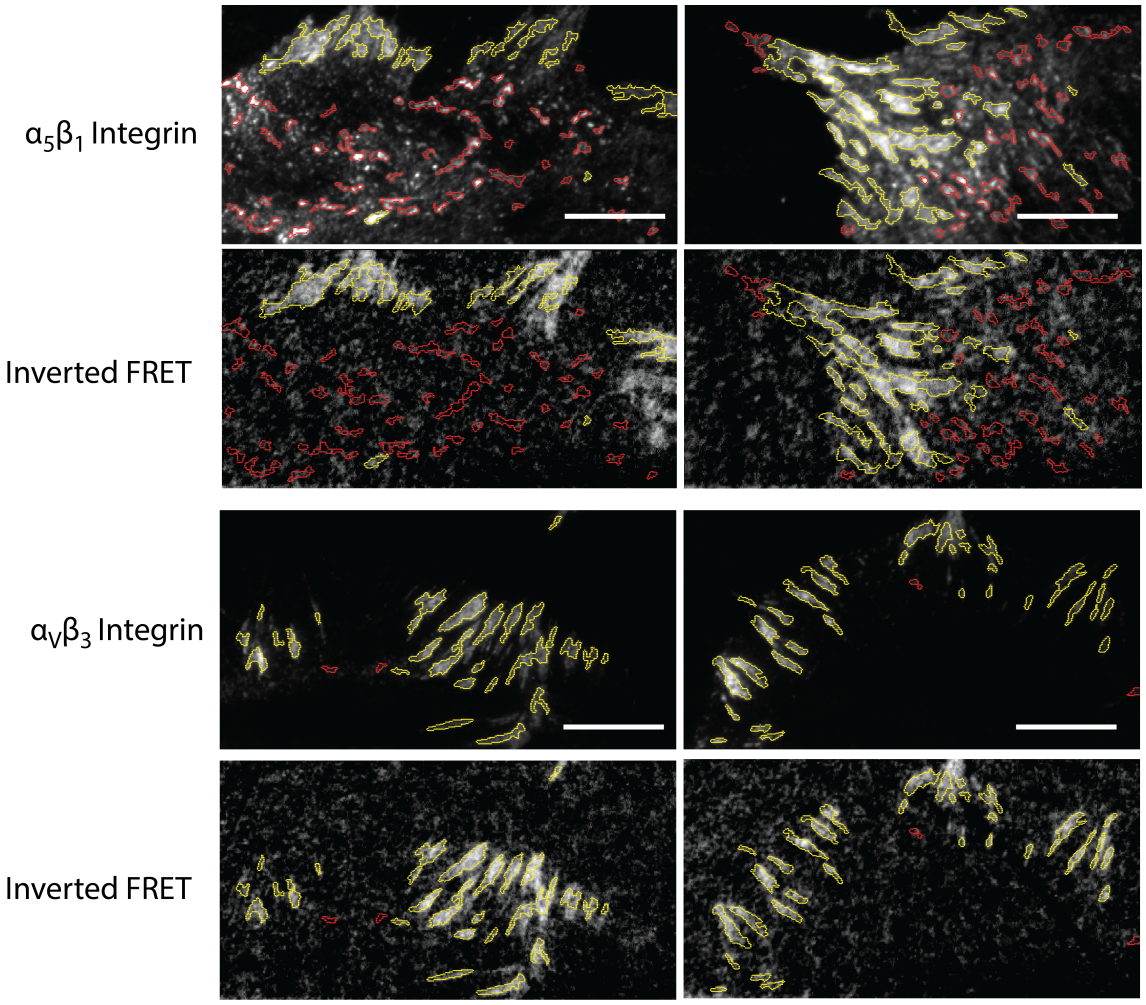

Figure S13. Detailed mapping and quantitative comparison between $\alpha_V\beta_3$ and $\alpha_5\beta_1$ colocalization, using immunocytochemistry to determine the location of endogenous integrins. Here we segment adhesions based on the Alexa 488 signal (corresponding to the 2° antibody used to stain for the specific integrin heterodimer). We then calculate the statistical difference between the FRET Index inside these adhesions as compared to FRET index elsewhere in the field of view. Yellow adhesions correspond to those whose average FRET Index value is at least 1 standard deviation below the average FRET Index value of the background. Red adhesions are those whose average FRET Index value is within 1 standard deviation of the background. To further quantify the correlation between integrin localization and force, we calculate the 2D correlation coefficient between the inverted FRET Index and integrin localization for the pixels with intensities above 20% of the Alexa 488 2°-Ab signal maximum. In addition, we calculate the 2D correlation coefficient between labeled antibody signal and inverted FRET index for all the pixels in a field of view.

Integrin	Number of cells	Correlation, 20% threshold Alexa 488 channel (+/- standard error on the mean)	Correlation for all pixels in field of view (+/- standard error on the mean)
$\alpha_5\beta_1$	5	0.39 +/- 0.09	0.56 +/- 0.06
$\alpha_V\beta_3$	7	0.52 +/- 0.05	0.78 +/- 0.03

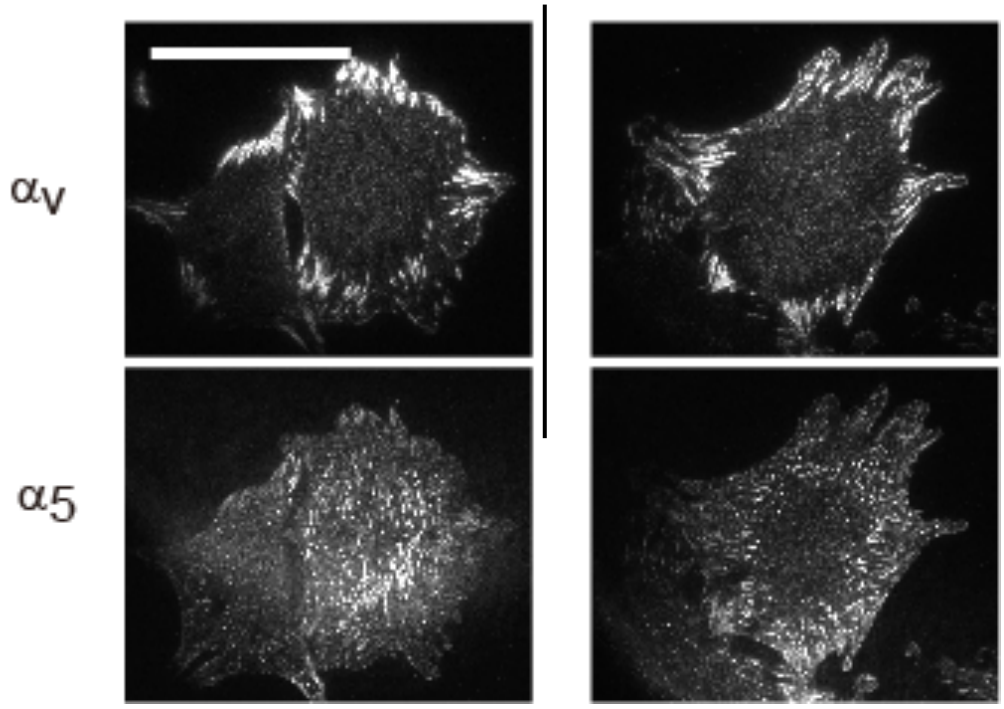

Figure S14. Immunofluorescence images of integrin α_5 and α_v. Cells plated on coverslips functionalized with MTSs were fixed with a solution of 4% paraformaldehyde (Polysciences, Inc.) in PBS, permeabilized with a solution of 0.25% Triton X-100 in PBS and blocked with a solution of 1% BSA in PBS. Samples were then incubated with 2 µg/mL primary antibodies (see "Antibodies" section for product details) overnight, washed, and then incubated with 1 µg/mL secondary antibodies (α_V: Dylight 649 conjugated antibody (Millipore, Cat# AP181SD), α_5: Alexa 488 conjugated antibody (Cell Signaling Technologies, Cat# 4412S)) for 30-60 min. Images are acquired with Hamamatsu sCMOS camera at 10 Hz. Scale bar is 65 µm.

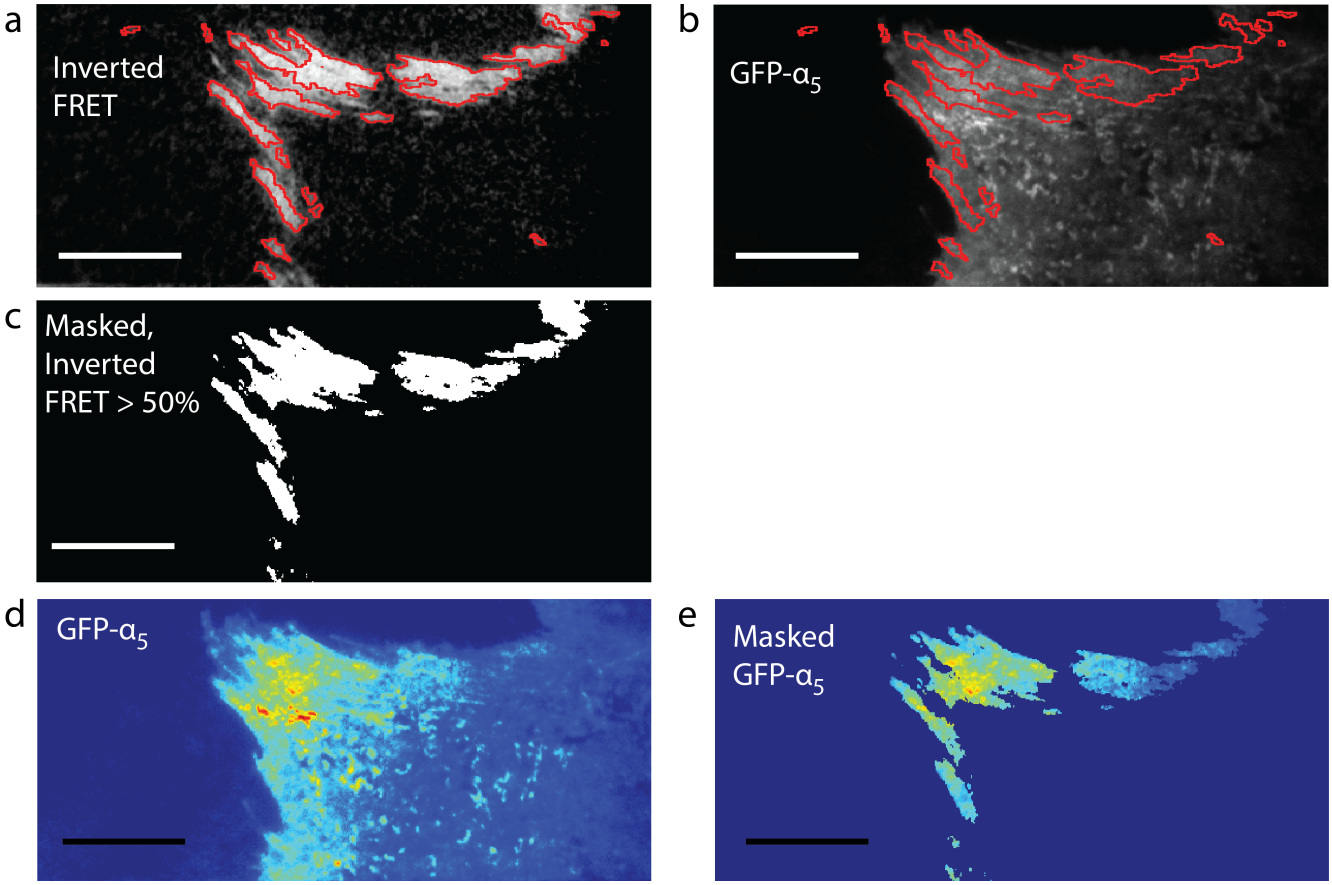

Figure S15. Quantification of GFP-α_5 and 2-D correlation with tension. For the images of GFP-α_5 we cannot use the same analysis used for the FA proteins and mEmerald-α_v because the adhesions outlined by GFP are not well defined. **a)** Thus, to calculate a correlation coefficient from the GFP-α_5 data, we first segment adhesion regions as defined by the inverted FRET image. **b)** We next calculate the 2D correlation between the FRET values and GFP values within these segmented adhesions. **c)** Alternatively, we threshold the inverted FRET image at 50% of the maximum, yielding a more inclusive mask. We then calculate the 2D correlation values between GFP intensity and inverted FRET index for all the pixels for each of the masking routines. Scale bar in all images = 10 µm.

Integrin	Number of cells	Number of adhesions	Correlation within adhesions (+/- standard error of the mean)	Correlation, 50% threshold (+/- standard error of the mean)
GFP-α_5	10	172	0.23 +/- 0.02	0.13 +/- 0.08
mEmerald-α_V	10	193	0.58 +/- 0.02	0.36 +/- 0.06

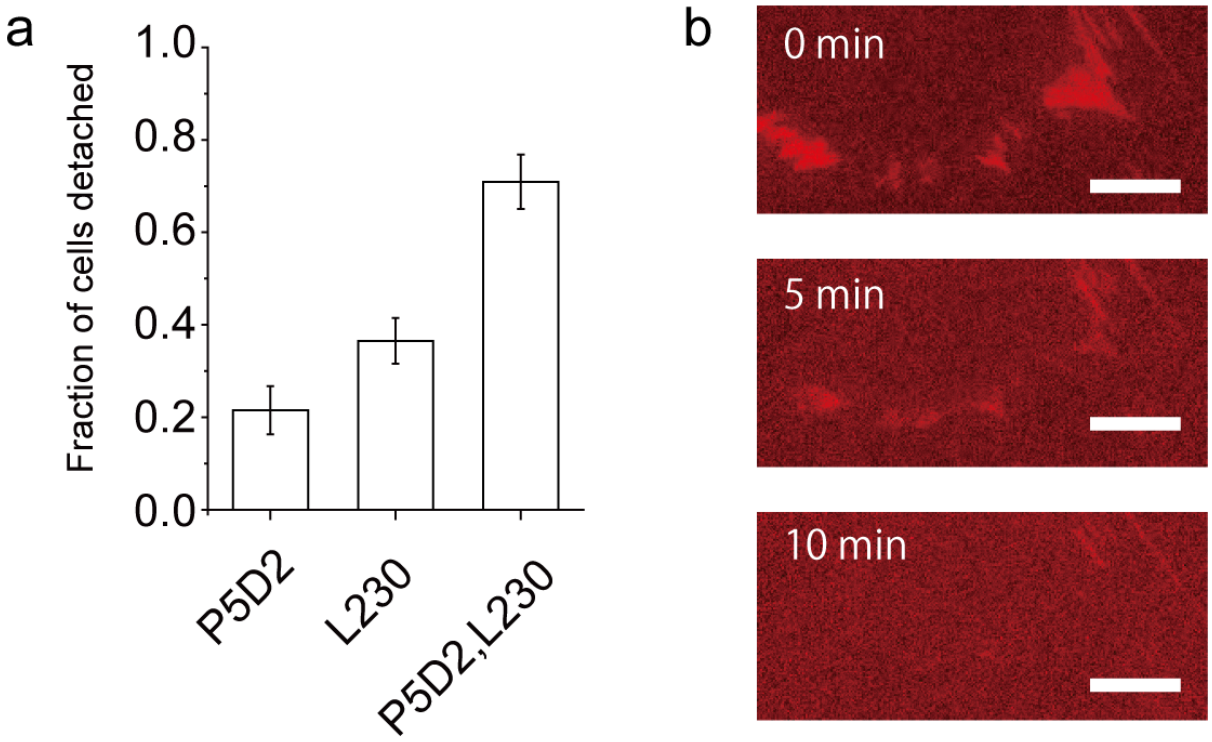

Figure S16. Blocking antibody experiments. **a)** The addition of blocking antibodies leads to cell detachment to differing degrees (P5D2: 1300 total cells over 4 fields of view, L230: 1000 total cells over 3 fields of view, P5D2+L230: 1500 total cells over 4 fields of view). Bar graph represents the mean and standard deviation for the different fields of view. **b)** Inverted FRET index maps acquired immediately after the addition of L230 (α_V blocking antibody), showing a dissipation of force.

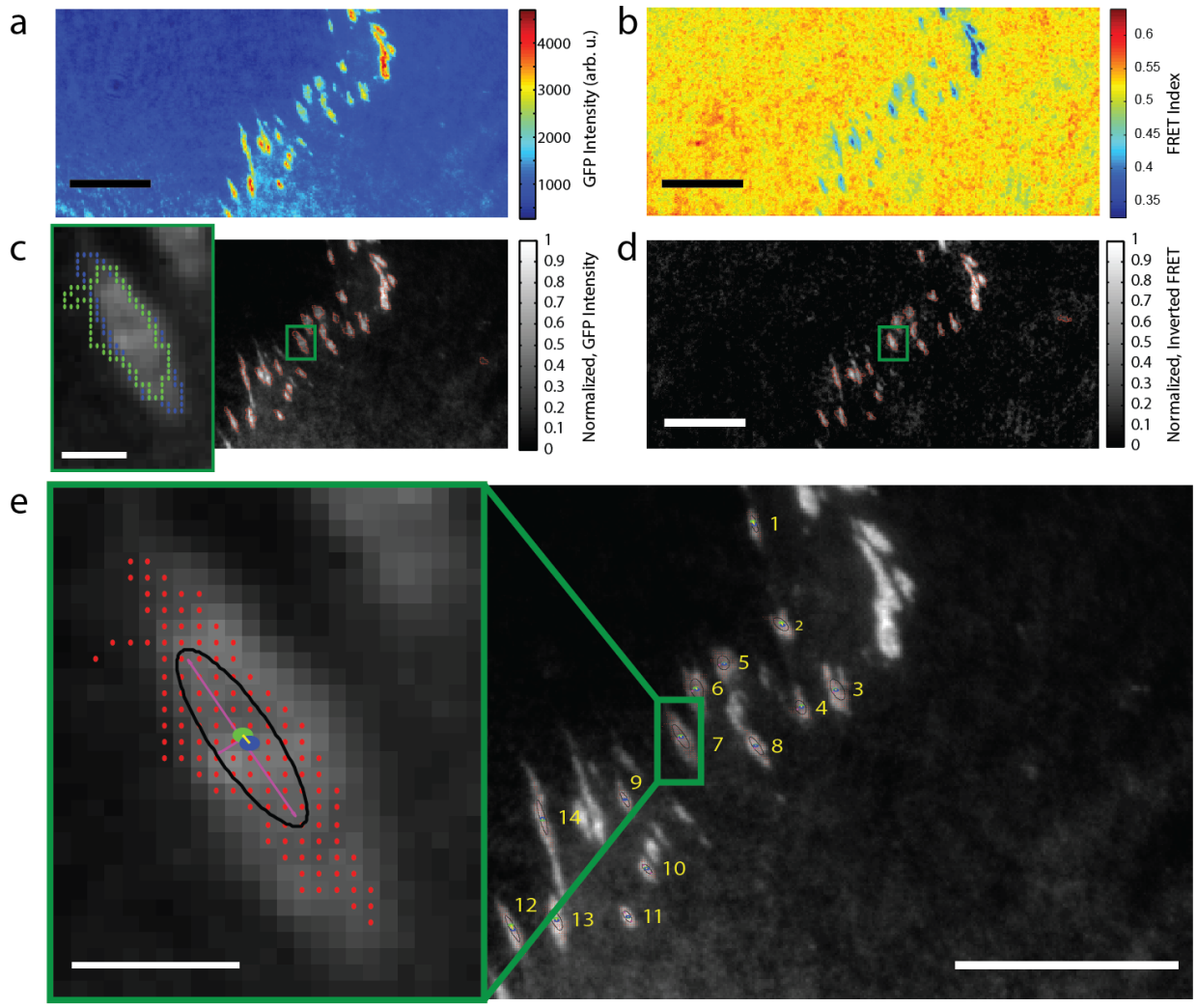

Figure S17. Schematic explanation of segmentation analysis. **a, b)** mEmerald-α_vHFF seeded on double-labeled MTSs and corresponding FRET Index map. **c, d)** Adhesions are segmented using a watershed algorithm and custom thresholding for both the normalized GFP image (c) and the inverted, normalized FRET image (d). The red lines represent the results of the segmentation. Regions are manually selected that correspond to isolated, correctly segmented adhesions. Inset shows a single adhesion. The blue and green outlines represent the result of the GFP and inverted FRET segmentation, respectively. The pixels within these outlined regions are combined for subsequent calculations. **e)** Results. Numbers represent adhesions that were manually selected from the watershed output. Inset: Red dots mark pixels included in the calculations. Black oval represents the ellipse best fit to the pixels. Pink lines represent major and minor axes of the ellipse. Blue and green dots are the centers of mass of GFP and inverted FRET, respectively. Yellow line is the vector between the two centers of mass. Scale bar in all figures is 10 µm. Scale bar in insets is 1 µm.

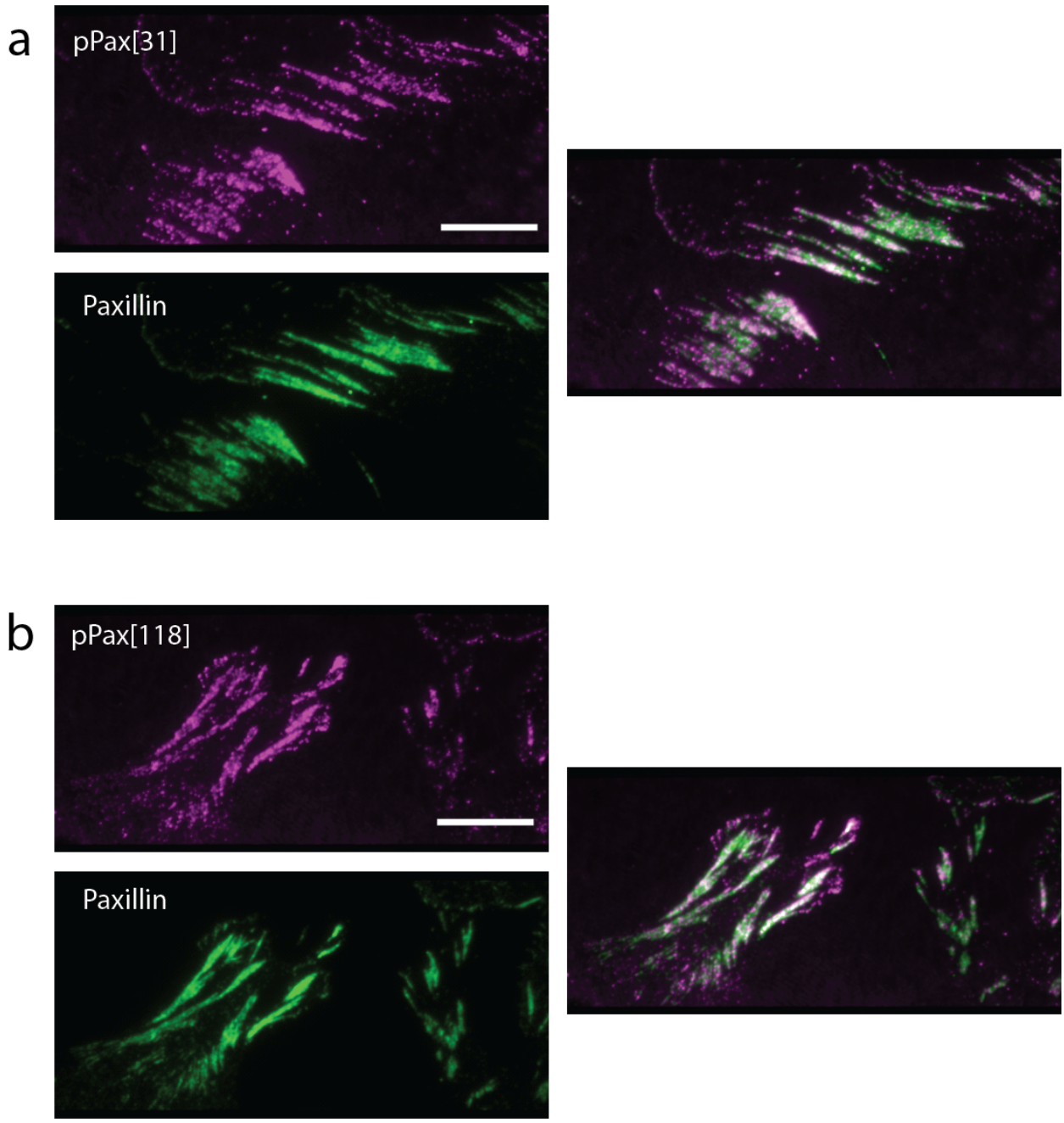

Figure S18. An HFF on an unlabeled MTS-coated coverslip fixed and stained for paxillin and phosphorylated paxillin Y31 and Y118. **a)** Phosphorylated paxillin (pY31) stained with secondary antibody conjugated with Alexa 488 (magenta). Total paxillin is stained with an Alexa 555 conjugated secondary (green). **b)** Phosphorylated paxillin (pY118) stained with secondary antibody conjugated with Alexa 488 (magenta). Total paxillin is stained with an Alexa 555 conjugated secondary antibody (green). Scale bar in all figures is 10 µm.

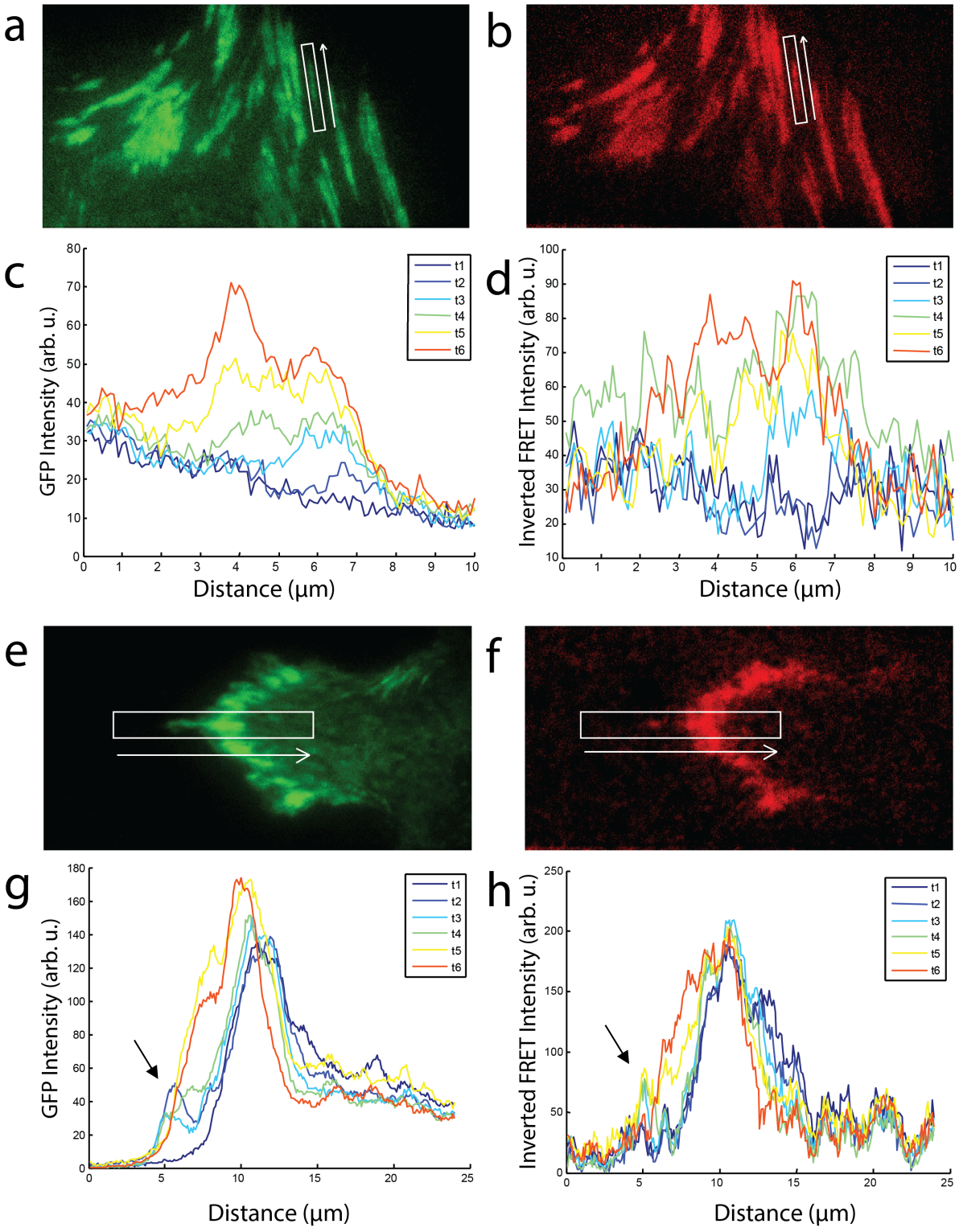

Figure S19. Representative line scans over the indicated regions for GFP-paxillin (a, c) and MTS-measured FRET (b, d) and for GFP-α-actinin (e, g) and MTS-measured FRET (f, h). In a-d, we see that the adhesion nucleates and grows; paxillin and FRET are qualitatively closely related in space and time. In e-h, we see the nucleation of an adhesion where α-actinin localization seemingly precedes force generation (see black arrow). Interval time is 1 minute.

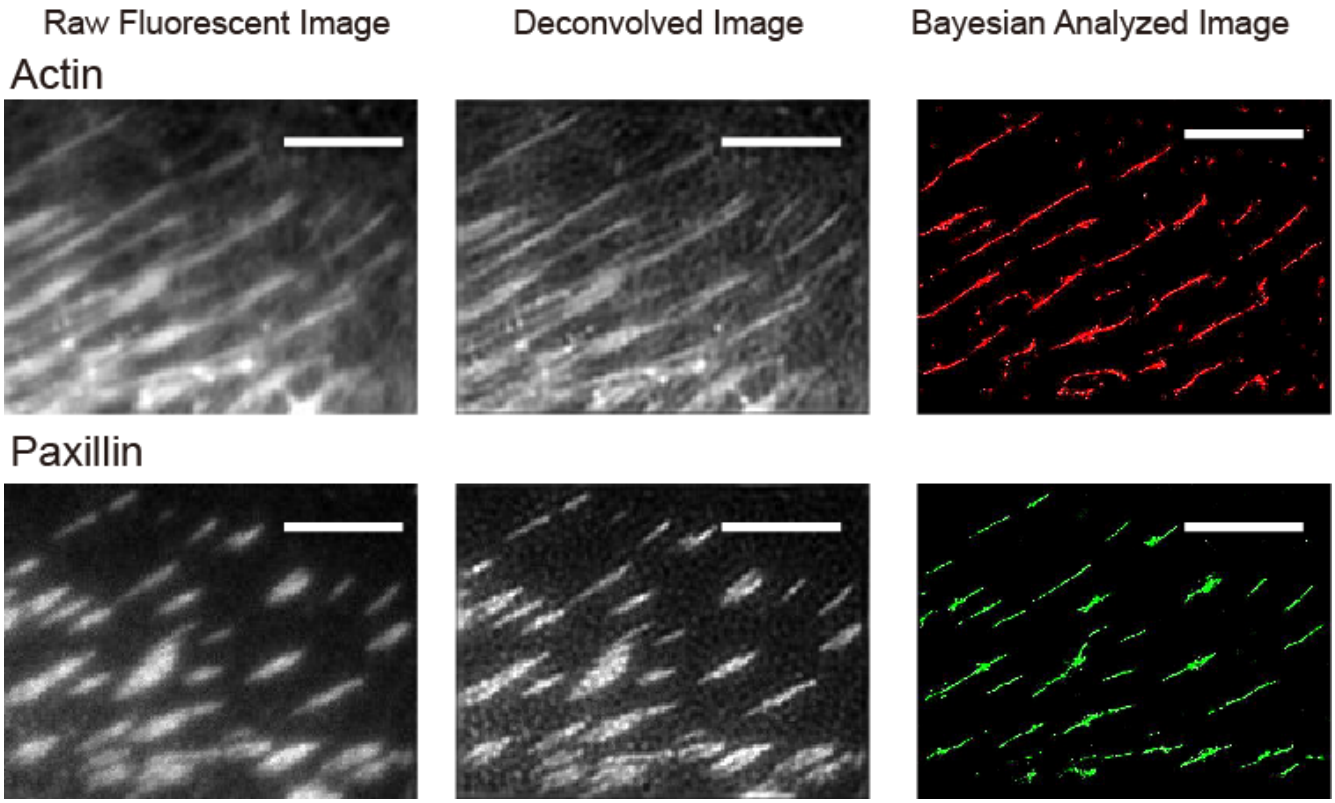

Figure S20. 3B and deconvolution images of actin (Alexa 555-phalloidin) and GFP-paxillin for an HFF seeded on unlabeled MTS-coated coverslips visualized via TIRF. Deconvolution was performed using the Lucy-Richardson algorithm[10] and an experimentally determined point-spread function with a full-width half-max of 1.3 pixels (130 nm). Scale bar in all images is 5 µm.

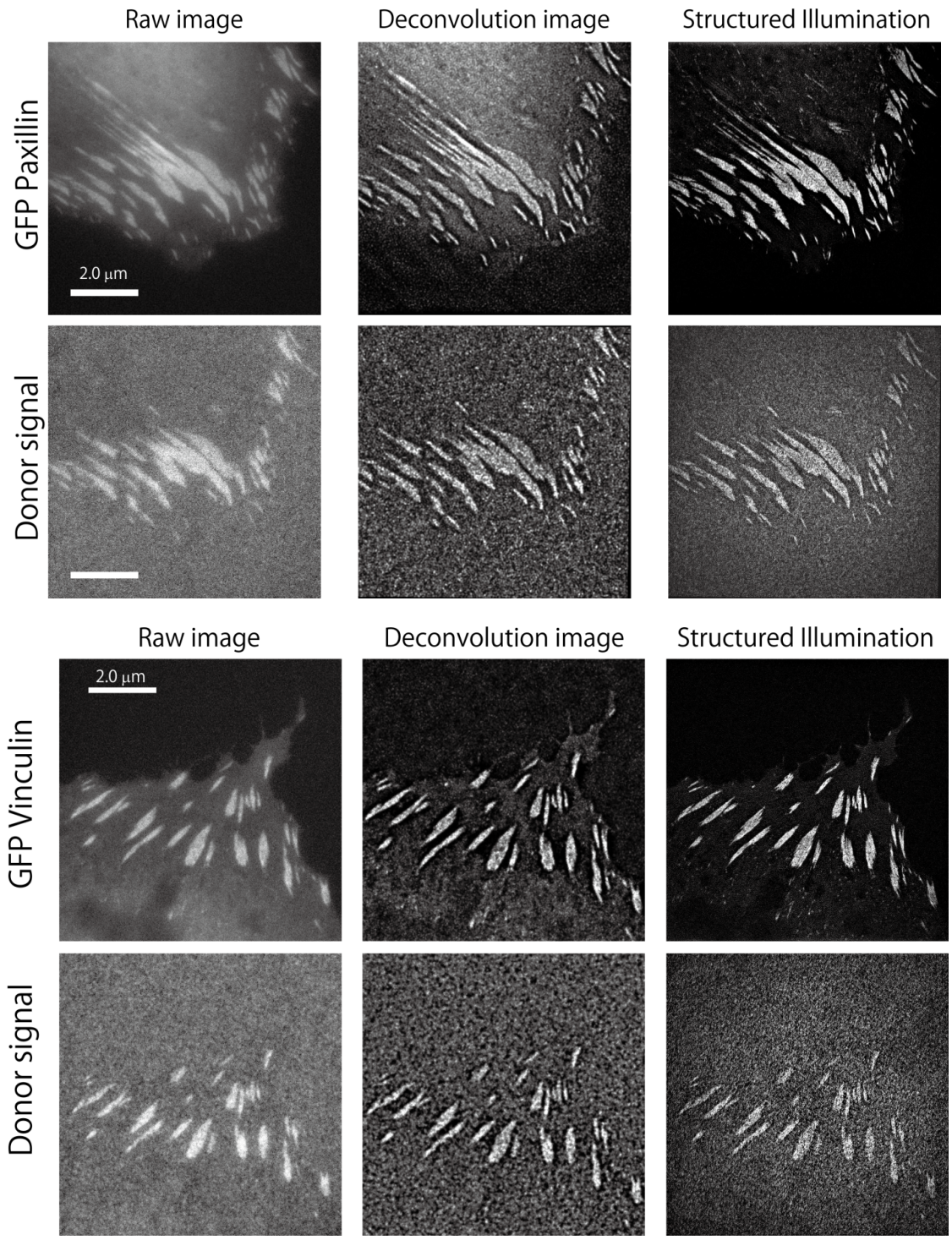

Figure S21. Structured Illumination Microscopy (SIM) images of GFP intensity and MTS-donor intensity recorded simultaneously. HFFs expressing GFP-paxillin or GFP-vinculin were plated on a MTS-coated coverslip. Constrained iterative 3D image restoration and image correction was done using the API/GE SoftWoRx deconvolution/SI reconstruction software package. Images were obtained using an Olympus 100x NA 1.4 oil immersion lens and imaging sampling using 125 nm z steps, and a 80 nm x, y raw pixel size. OMZ BLAZE SI patterns were generated using a GE proprietary electro-optical high-speed SI diffraction grating engine. Scale bar in all figures is 2 μm.

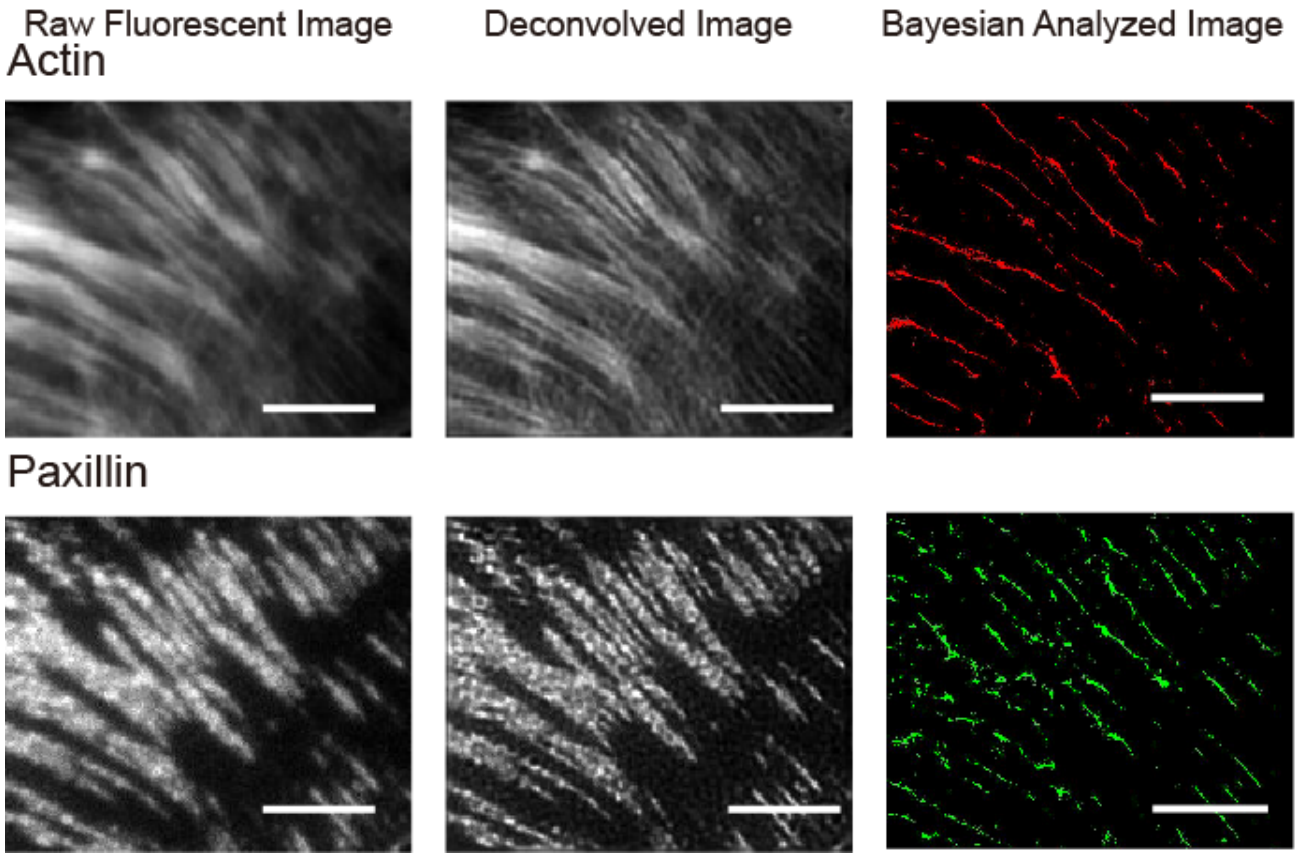

Figure S22. 3B and deconvolution images of actin (Alexa 555-phalloidin) and GFP-paxillin for an HFF seeded on fibronectin-coated coverslips visualized via TIRF. Deconvolution was performed using the Lucy-Richardson algorithm[22] and an experimentally determined point-spread function with a full-width half-max of 1.3 pixels (130 nm). Scale bar in all images is 5 µm.

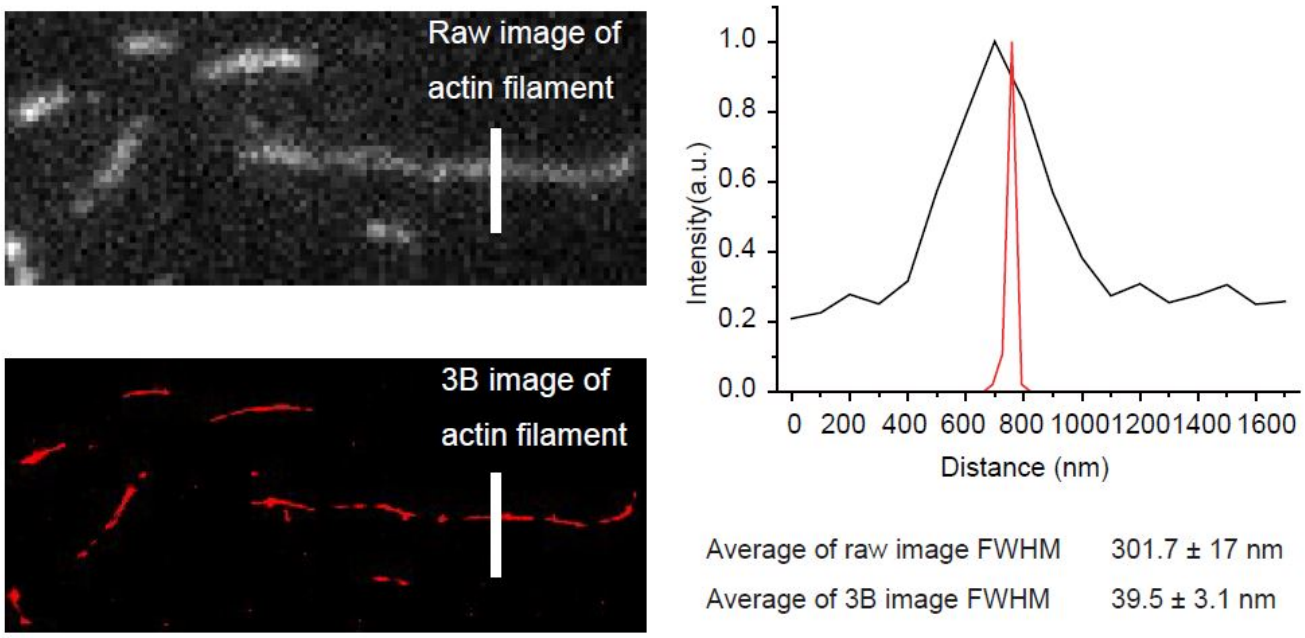

Figure S23. Single actin filaments resolved by 3B analysis. Raw images (gray) and 3B reconstructed images (red) of tetramethylrhodamine (TMR)-labeled actin filaments adhered to a microscope coverslip. Methods: G-actin and biotinylated G-actin (10:1) were copolymerized with TMR-phalloidin. ~15 nM TMR-labeled actin filaments were then immobilized on biotin-PEG coated coverslips (MicroSurfaces, Inc.) via Neutravidin. A representative line scan of a single actin filament shows the spatial resolution of the raw image and the 3B reconstructed image. A Gaussian fit to similar line scans (13 lines) yields an average FWHM 39.5 ± 3.1 nm (SEM). The theoretical spatial resolution is $0.61 \times \lambda/\mathrm{NA}$ or 0.61 x 532 nm/1.49 = 217.8 nm.

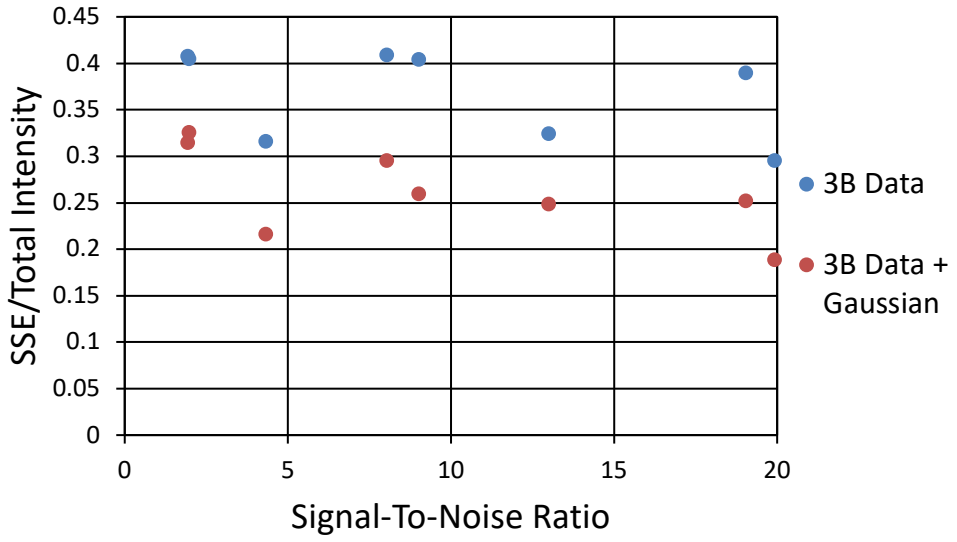

Figure S24. Calculation of SSE with respect to image SNR for 3B analysis. Lower SSE indicates better agreement between the 3B image and the original data. A clear trend in SSE as a function of SNR in the original data is not readily apparent. The blue dots represent the SSE between the result of the 3B analysis and the normalized original data. The red dots represent the SSE between the result of the 3B analysis with a 2D Gaussian convolved with the resolved positions of the fluorophores and the normalized original data (See *Quantification of 3B Analysis).*

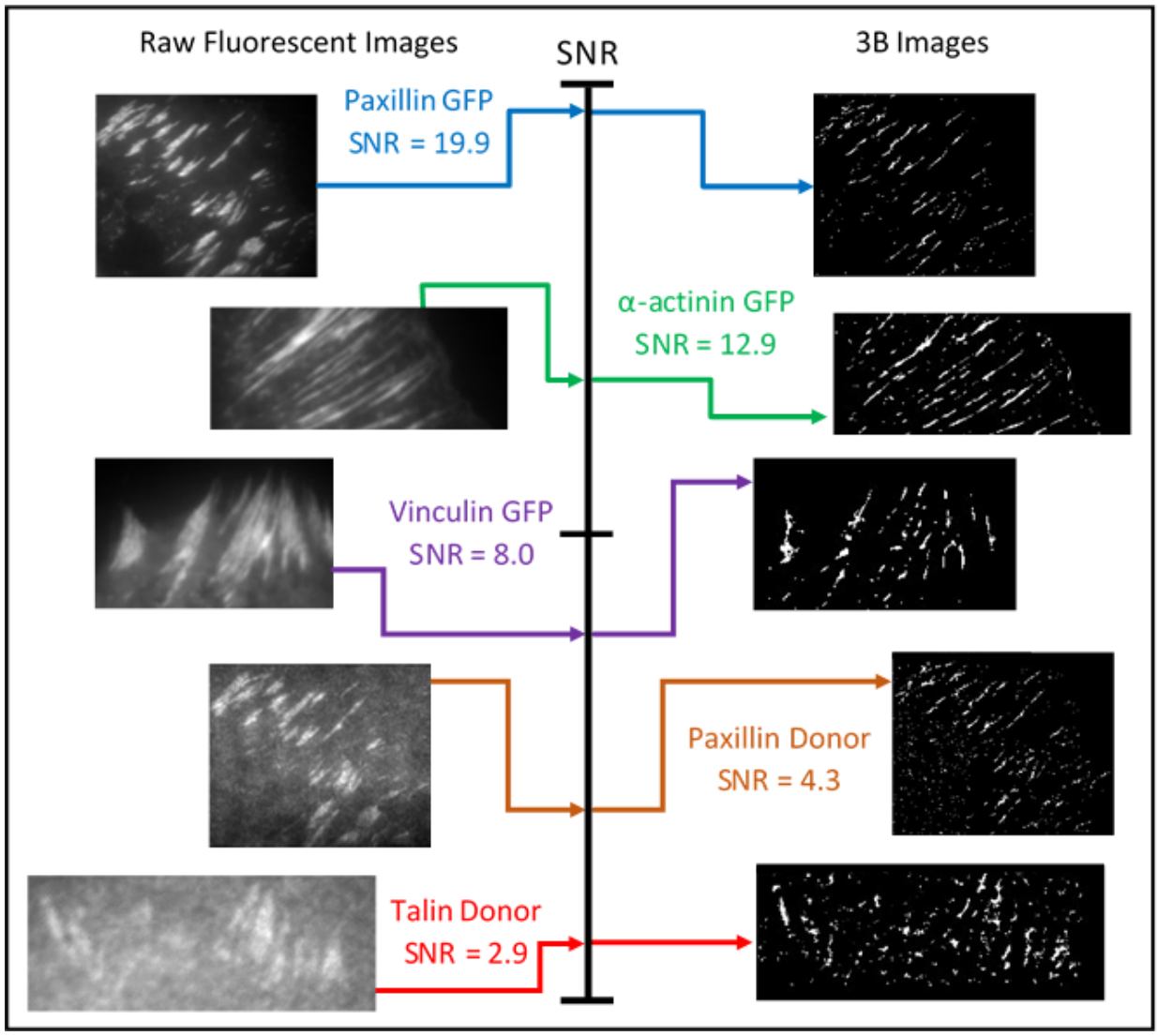

Figure S25. Example images comparing raw fluorescence data and resolved, 3B images. Paxillin donor and talin donor denotes the FRET donor channels recorded in the presence of GFP-paxillin and GFP-talin, respectively. Instances of high FRET donor emission in the 3B images that do not obviously correspond to FAs may reflect MTS molecules lacking the FRET acceptor, transient local tension generating events, or statistical fluctuations in the data.

Video S1. Time-lapse FRET data acquired at 1 frame every 20 seconds with a 250 ms exposure per frame. Low FRET regions appear black and correspond to high traction force.

Video S2. FRET signal and GFP-MRLC acquired simultaneously after the addition of 50 μM ML-7 (myosin light chain kinase inhibitor). Top panel is inverted FRET (bright represents high force), middle panel is GFP-MRLC, and bottom panel is merged (red is inverted FRET and green is GFP). Data is taken at 1 frame every 30 seconds with a 500 ms exposure per frame. The response is dose-dependent, as 10 μM ML-7 resulted in a slower abrogation of FRET signal as compared to the results observed with 100 μM ML-7, in which we observed almost complete abrogation of tension production within 2 minutes (data not shown).

Video S3. Time-lapse FRET data acquired simultaneously with GFP-α-actinin. Top panel is inverted FRET (bright represents high force), middle panel is GFP-α-actinin, and bottom panel is merged (red is inverted FRET and green is GFP). Data is taken at 1 frame every 60 seconds with a 500 ms exposure per frame.

Video S4. Time-lapse FRET data acquired simultaneously with GFP-paxillin. Top panel is inverted FRET (bright represents high force), middle panel is GFP-paxillin, and bottom panel is merged (red is inverted FRET and green is GFP). Data is taken at 1 frame every 60 seconds with a 500 ms exposure per frame.

Video S5. Example 3B raw data. GFP-Paxillin (left panel) and FRET donor (right panel) movies were acquired at 20 frames per second for 150 frames, with a 50 ms exposure per frame. The laser power is adjusted to ensure significant photobleaching and photoblinking over the duration of the 150 frames.

References

(1) Hu, K.; Ji, L.; Applegate, K. T.; Danuser, G.; Waterman-Storer, C. M. *Science* **2007**, *315*, 111–115.

(2) Laukaitis, C. M.; Webb, D. J.; Donais, K.; Horwitz, A. F. *J. Cell Biol.* **2001**, *153*, 1427–1440.

(3) Chen, L.; Vicente-Manzanares, M.; Potvin-Trottier, L.; Wiseman, P. W.; Horwitz, A. R. *PLoS One* **2012**, *7*.

(4) Huebsch, N.; Arany, P. R.; Mao, A. S.; Shvartsman, D.; Ali, O. A.; Bencherif, S. A.; Rivera-Feliciano, J.; Mooney, D. J. *Nat. Mater.* **2010**, *9*, 518–526.

(5) Richman, G. P.; Tirrell, D. A.; Asthagiri, A. R. *J. Controlled Release* **2005**, *101*, 3–12.

(6) Rantala, J. K.; Pouwels, J.; Pellinen, T.; Veltel, S.; Laasola, P.; Mattila, E.; Potter, C. S.; Duffy, T.; Sundberg, J. P.; Kallioniemi, O.; Askari, J. A.; Humphries, M. J.; Parsons, M.; Salmi, M.; Ivaska, J. *Nat. Cell Biol.*, **2011**, *13*, 1315–1324.

(7) Spiczka, K. S.; Yeaman, C. *J. Cell Sci.* **2008**, *121*, 2880–2891.

(8) Comeau, J. W.; Kolin, D. L.; Wiseman, P. W. *Mol. Biosyst.* **2008**, *4*, 672–685.

(9) Kanchanawong, P.; Shtengel, G.; Pasapera, A. M.; Ramko, E. B.; Davidson, M. W.; Hess, H. F.; Waterman, C. M. *Nature* **2010**, *468*, 580–584.

(10) Case, L. B.; Waterman, C. M. *PLos One* **2011**, *6*, e26631.

(11) Waxmonsky, N. C.; Conner, S. D. *J. Cell Sci.*, **2013**, *126* , 3593–3601.

(12) Stadler, C.; Rexhepaj, E.; Singan, V. R.; Murphy, R. F.; Pepperkok, R.; Uhlén, M.; Simpson, J. C.; Lundberg, E. *Nat. Methods* **2013**, *10*, 315–323.

(13) Chin, J. W.; Santoro, S. W.; Martin, A. B.; King, D. S.; Wang, L.; Schultz, P. G. *J. Am. Chem. Soc.* **2002**, *124*, 9026–9027.

(14) Roy, R.; Hohng, S.; Ha, T. *Nat. Methods* **2008**, *5*, 507–516.

(15) Zamir, E.; Katz, B. Z.; Aota, S.; Yamada, K. M.; Geiger, B.; Kam, Z. *J. Cell Sci.* **1999**, *112 (Pt 1*, 1655–1669.

(16) Berney, C.; Danuser, G. *Biophys. J.* **2003**, *84*, 3992–4010.

(17) McCann, J. J.; Choi, U. B.; Zheng, L.; Weninger, K.; Bowen, M. E. *Biophys. J.* **2010**, *99*, 961–970.

(18) Cox, S.; Rosten, E.; Monypenny, J.; Jovanovic-Talisman, T.; Burnette, D. T.; Lippincott-Schwartz, J.; Jones, G. E.; Heintzmann, R. *Nat. Methods* **2012**, *9*, 195–200.

(19) Hu, Y. S.; Nan, X.; Sengupta, P.; Lippincott-Schwartz, J.; Cang, H. *Nat. Methods* **2013**, *10*, 96–97.

(20) Westphal, V.; Rizzoli, S. O.; Lauterbach, M. A.; Kamin, D.; Jahn, R.; Hell, S. W. *Science* **2008**, *320*, 246–249.

(21) Morimatsu, M.; Mekhdjian, A. H.; Adhikari, A. S.; Dunn, A. R. *Nano Lett.* **2013**, *13*, 3985–3989.

(22) Biggs, D. S.; Andrews, M. *Appl. Opt.* **1997**, *36*, 1766–1775.